



# 1 ET-WB: water balance-based estimations of terrestrial evaporation 2 over global land and major global basins

3 Jinghua Xiong<sup>1#</sup>; Abhishek<sup>2#</sup>; Li Xu<sup>3</sup>; Hrishikesh A. Chandanpurkar<sup>3</sup>; James S. Famiglietti<sup>3,4</sup>; Chong  
4 Zhang<sup>5</sup>; Gionata Ghiggi<sup>6</sup>; Shenglian Guo<sup>1</sup>; Yun Pan<sup>5</sup>; Bramha Dutt Vishwakarma<sup>7,8</sup>

5 <sup>1</sup>State Key Laboratory of Water Resources and Hydropower Engineering Science, Wuhan University, Wuhan, 430072, Hubei,  
6 China

7 <sup>2</sup>Department of Civil Engineering, Indian Institute of Technology Roorkee, Roorkee 247667, India

8 <sup>3</sup>University Saskatchewan, Global Institute for Water Security, Saskatoon, SK S7N 3H5, Canada

9 <sup>4</sup>Arizona State University, Global Futures Laboratory, Tempe, AZ, 85281, United States

10 <sup>5</sup>Beijing Laboratory of Water Resources Security, Capital Normal University, Beijing, 100048, China

11 <sup>6</sup>Environmental Remote Sensing Laboratory (LTE), EPFL, 1005 Lausanne, Switzerland

12 <sup>7</sup>Interdisciplinary Centre for Water Research, Indian Institute of Science, Bengaluru, 560012, India

13 <sup>8</sup>Centre for Earth Sciences, Indian Institute of Science, Bengaluru, 560012, India

14

15 *#Jinghua Xiong and Abhishek contributed equally.*

16 *Correspondence to:* Shenglian Guo (slguo@whu.edu.cn); Yun Pan (pan@cnu.edu.cn)

17

## 18 **Abstract**

19 Evaporation (ET) is one of the crucial components of the water cycle, which serves as the nexus between global water, energy,  
20 and carbon cycles. Accurate quantification of ET is, therefore, pivotal in understanding various earth system processes and  
21 subsequent societal applications. The prevailing approaches for ET retrievals are either limited in spatiotemporal coverage or  
22 largely influenced by choice of input data or simplified model physics, or a combination thereof. Here, using an independent  
23 mass conservation approach, we develop water balance-based ET datasets (ET-WB) for the global land and the selected 168  
24 major river basins. We generate 4669 probabilistic unique combinations of the ET-WB leveraging multi-source datasets (23  
25 precipitation, 29 runoff, and 7 storage change datasets) from satellite products, in-situ measurements, reanalysis, and  
26 hydrological simulations. We compare our results with the four auxiliary global ET datasets and previous regional studies,  
27 followed by a rigorous discussion of the uncertainties, their possible sources, and potential ways to constrain them. The  
28 seasonal cycle of global ET-WB possesses a unimodal distribution with the highest (median value: 65.61 mm/month) and  
29 lowest (median value: 36.11 mm/month) values in July and January, respectively, with the spread range of roughly  $\pm 10$   
30 mm/month from different subsets of the ensemble. Auxiliary ET products illustrate similar intra-annual characteristics with  
31 some over/under-estimation, which are completely within the range of the ET-WB ensemble. We found a gradual increase in  
32 global ET-WB from 2003 to 2010 and a subsequent decrease during 2010-2015, followed by a sharper reduction in the  
33 remaining years primarily attributed to the varying precipitation. Multiple statistical metrics show reasonably good accuracy



34 of monthly ET-WB (e.g., a relative bias of  $\pm 20\%$ ) in most river basins, which ameliorates at annual scales. The long-term  
35 mean annual ET-WB varies within 500-600 mm/yr and is consistent with the for auxiliary ET products (543-569 mm/yr).  
36 Observed trend estimates, though regionally divergent, are evidence of the increasing ET in a warming climate. The current  
37 dataset will likely be useful for several scientific assessments centering around water resources management to benefit society  
38 at large. The dataset is publicly available at <https://doi.org/10.5281/zenodo.7314920> (Xiong et al., 2023).

39

## 40 **1 Introduction**

41 Land evaporation (ET), the total amount of water evaporating from the land surface to the atmosphere, is a crucial component  
42 of the terrestrial water cycle (Rodell et al., 2015; Wang and Dickinson, 2012). It includes the water evaporating from the bare  
43 soil, open water bodies, canopy-intercepted precipitation, sublimation, and transpiration from the plant stomata (Miralles et  
44 al., 2020). Since the global ET returns about two-thirds of the land precipitation back to the atmosphere, it sustains the water  
45 cycle by providing the moisture supply for precipitation and directly affects the partitioning of the Earth's surface heat fluxes  
46 and subsequent heating and cooling effects (Good et al., 2015; Koster et al., 2004; Oki and Kanae, 2006). Thus, ET links the  
47 Earth's surface and the atmosphere and acts as the key element for the interconnected global water, energy, and carbon cycles  
48 (Jung et al., 2010). Accurate quantification of ET is, therefore, imperative for studying the water cycle changes, freshwater  
49 availability and demand, weather and climate dynamics, earth system processes, and surface energy budget closures. However,  
50 ET is poorly constrained, especially at large scales compared to the other components of the water cycle (Syed et al., 2010;  
51 Jasechko et al., 2013; Chandanpurkar et al., 2017), which may become more uncertain with an intensifying hydrological cycle  
52 under a warming climate. To this end, the trends and variability of the global ET fluxes still remain contested (Dong and Dai,  
53 2017; Fisher et al., 2017; Pascolini-Campbell et al., 2020).

54 Over the past few decades, ET-based science has advanced significantly across scales from leaf to global scales  
55 (Fisher et al., 2017). Several ET products derived from the data-driven and data assimilation methods, satellite observations,  
56 and simulations from the physically or empirically based land surface models have been developed (Long et al., 2014; Liu et  
57 al., 2016); a community effort that is still ongoing (Miralles et al., 2016). These ET products are dedicated to minimizing the  
58 existing shortcomings stemming from varying spatiotemporal scales and are tailored to specific forcing variables (Miralles et  
59 al., 2016). For example, Moderate Resolution Imaging Spectroradiometer (MODIS) ET data provides regular 1 km<sup>2</sup> land  
60 surface ET over 109.03 million km<sup>2</sup> of global vegetated land areas at 8-day, monthly and annual intervals (Mu et al., 2011).  
61 Also, recent deep learning-based methods have shown an enhanced ability for global ET estimation when compared against  
62 proxy estimates from satellite observations and sparse in-situ data (Koppa et al., 2022). Despite the large spatial and temporal  
63 scale ET retrievals, all of these datasets inherently possess several uncertainties originating either from the forcing datasets or  
64 propagated uncertainty through the varying model structures or a combination thereof. For example, accurate estimations of  
65 ET utilizing the land surface temperature (LST) or other satellite optical and thermal observations need clear skies and hence



66 are limited in temporal coverage due to the cloud cover issues (Long et al., 2014; Wang and Dickinson, 2012; Yang and Shang,  
67 2013). Similarly, the mismatch between the spatial scales of the forcing data and the vegetation data, in the case of the  
68 Normalized Difference Vegetation Index-based ET products, can result in large uncertainties (Yang et al., 2013).

69 Owing to all these uncertainties associated with the different methodological approaches, model assumptions, and  
70 scaling issues, the resulting observed ET estimates and their future projections have huge variations from product to product  
71 (Liu et al., 2016; Wang and Dickinson, 2012; Wang et al., 2015). Such disparities generally impede selecting the most  
72 appropriate ET data and even make it contentious, at times, for their application in various hydrometeorological modeling  
73 studies, management, or policymaking frameworks, among others. Moreover, the traditional estimations and the standards for  
74 the validation of ET solely from ground-based measurements from, for example, lysimeters and eddy covariance flux towers,  
75 are also insufficient for larger basin-scale evaluations because of the sparsely distributed network (Pascolini-Campbell et al.,  
76 2020; Wang and Dickinson, 2012). Such limited point observations can further lead to high spatiotemporal heterogeneity  
77 variability in the ET, suffering mainly from the uncertainties arising from the data gap filling and upscaling beyond their  
78 representative local areas (Liu et al., 2016; Pascolini-Campbell et al., 2020). Therefore, in the context of a changing climate  
79 and continually intensifying human activities, the paramount importance of ET in global and regional water cycles and  
80 associated land-atmosphere interactions fosters the need and underscores the importance of independent, large-scale, and  
81 better-constrained ET estimates.

82 Since the multifaceted variable, ET, is difficult to measure from space or from in-situ records directly, it has to be  
83 derived through the physically driven models incorporating a variety of controlling atmospheric, radiative, and vegetative  
84 factors (Fisher et al., 2017). However, the recent advancement in mapping the other components of the water cycle, changes  
85 in the terrestrial water storage (TWS), in particular, has enabled an alternate assessment of ET at large basin scales, which  
86 often is the scale of interest in water resources management (Pascolini-Campbell et al., 2020). The Gravity Recovery And  
87 Climate Experiment (GRACE) and its successor GRACE Follow-On (both jointly referred to as GRACE hereafter) have  
88 provided the TWS (sum of all of the water storage components within a land mass) variations with unprecedented accuracy  
89 since 2002 (Tapley et al., 2004; Sneeuw et al., 2014; Rodell et al., 2018). When used in combination with the precipitation and  
90 runoff in a water balance equation, the changes in TWS can be used for an independent and mass conservation-based estimate  
91 of ET, which will be free from most of the above-mentioned shortcomings in the modeled, upscaled, or in-situ products (Rodell  
92 et al., 2004; Bhattarai et al., 2019). Moreover, the resulting ET will be better constrained since the GRACE inferred TWS  
93 contains the embedded signals of both the natural variability and the anthropogenic influences. The major limitation with  
94 GRACE TWS variations is, however, its coarse spatial resolution (Ramillien et al., 2006) which we take the edge off by  
95 limiting our analysis to the global land and major global basins.

96 Previous studies employing the water balance approach either rely on single datasets of precipitation and/or runoff  
97 (Gibson et al., 2019; Liu et al., 2016) are focussed on the regional scales (Castle et al., 2016; Pascolini-Campbell et al., 2020;



98 Rodell et al., 2004; 2011; Swann et al., 2017; Wan et al., 2015). A few global studies (e.g., Liu et al., 2016; Miralles et al.,  
99 2016; Ramillien et al., 2006; Zeng et al., 2012; Lehmann et al., 2022) are limited either in terms of data used or in the temporal  
100 coverage. Here, we leverage a multitude of precipitation, runoff, and TWS changes (23, 29, and 7, respectively) datasets and  
101 employ the water balance approach to generate a total of 4669 subsets of ET during 2002-2021 for global land and major 168  
102 river basins. We rigorously assess the uncertainty bounds of the resulting ET and also analyze the relationship with various  
103 attributes such as the basin area, climate (aridity index, AI), and human interventions (irrigation). This water balance approach  
104 checks global and basin scale ET given the spatial accumulation of errors in LSM- or RS-based ET products (Pascolini-  
105 Campbell et al., 2020). Given the ongoing controversy over the reliability of existing ET products, while in situ observation  
106 data are scarce (Douville et al., 2013; Zhang et al., 2016), the inter-comparison of mass-balance derived monthly ET ensemble  
107 estimates with several existing ET datasets provides a way to benchmark and improve the estimate of ET. We expect our  
108 product will be relevant for various scientific and societal applications, including the study of extreme events, water and carbon  
109 cycle, agricultural management, sea level budgeting, biodiversity assessments, global and regional hydrological cycle, water  
110 resources management, ecosystem resilience, and for improving weather predictions across scales (Fisher et al., 2017).

## 111 2 Methods

### 112 2.1 Water balance equation

113 The terrestrial water balance method was used to produce the ET-WB dataset. For a basin scale, it can be written as follows:

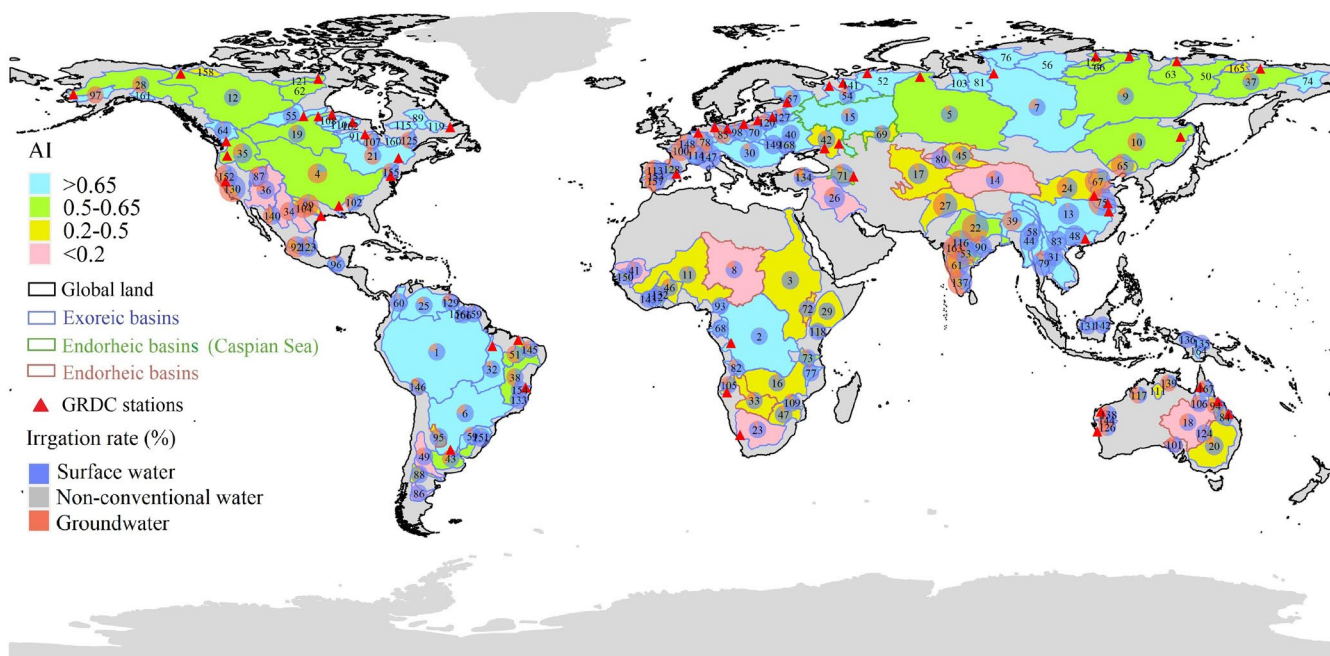
$$114 \quad ET = P - \Delta S - R \pm WD \quad (1)$$

115 where P is the basin-averaged precipitation, and R is the river flow or runoff going outside the basin.  $\Delta S$  is the monthly storage  
116 change which is calculated as the backward difference of the terrestrial water storage (i.e., the changes in the month of  
117 calculation and the previous month), while different computation methods, such as the backward difference combined with a  
118 three-month running average might produce subtle difference (Long et al., 2014; Pascolini-Campbell et al., 2020). WD denotes  
119 the diverted water volume inside/outside the basin. All the water fluxes are on the monthly scale from May 2002 to December  
120 2021 and expressed in the unit of millimeters (mm/month) of equivalent water depth. WD is not considered in our study  
121 because the amplitude of the transferred water of most projects is generally small relative to other water components and/or  
122 directly flows outside the basin through the river channels. Therefore, the WD influences on the water balance ET estimations  
123 might be considered small, even for the 14 major existing projects located across the 168 studied basins from the Global Water  
124 Transfer Megaprojects depository (Shumilova et al., 2018) (Table S1). Although the terrestrial water balance method has been  
125 extensively applied in different river basins of the world (Rodell et al., 2004; Long et al., 2014; Li et al., 2019), a global  
126 database is still lacking, and the systematic uncertainty, variation, and distribution also remain unexplored from a global  
127 perspective.



128 We performed the calculation over the 168 major river basins of the world from the Global Runoff Data Centre  
129 (GRDC, [https://www.bafg.de/GRDC/EN/Home/homepage\\_node.html](https://www.bafg.de/GRDC/EN/Home/homepage_node.html)) and the global land excluding Antarctic and Greenland  
130 (Fig. 1). These selected basins cover a wide range of climate conditions and human intervention with a minimum area of  
131  $\sim 64,000$  km<sup>2</sup>, which is sufficiently large for the retrieval of TWSA from GRACE solutions at basin scale at least in the  
132 hydrology community (Vishwakarma et al., 2018). Apart from the terrestrial water balance, the atmospheric water balance  
133 also offers an effective alternative framework to estimate ET as it is also an important factor in the atmospheric water cycle,  
134 i.e., the residual precipitation, the horizontal divergence of the vapor flux, and the change in column water vapor. Although  
135 such an alternative estimation of ET from the independent atmospheric data can potentially supplement the water balance-  
136 based ET (referred to as ‘ET-WB’ hereafter), this is outside the scope of our study.

137



138

139 **Figure 1: Location and attributes of the 168 studied river basins. The labeled numbers represent the basin ID. Please find further**  
140 **details in Table S2. The irrigation information is obtained from the latest version of the Food and Agricultural Organization (FAO)**  
141 **Global Map of Irrigated Areas ([https://www.fao.org/aquastat/en/geospatial-information/global-maps-irrigated-areas/latest-](https://www.fao.org/aquastat/en/geospatial-information/global-maps-irrigated-areas/latest-version/)**  
142 **version/). The aridity index information is collected from the Version 3 of the Global Aridity Index and Potential Evapotranspiration**  
143 **Database (Zomer et al., 2022). The inserted pie chart indicates the percentage of irrigation area from different water sources to the**  
144 **basin area. The radii are proportional to the total percentage of the equipped irrigation area, which has been re-scaled using the**  
145 **natural logarithms after adding 10 to avoid negative (very small) values for better visualisation.**

## 146 2.2 Evaluation metrics

147 The ET-WB dataset was compared with multiple global ET products (see details in the Data section) at various temporal and  
148 spatial scales. Firstly, the comparisons were conducted at the monthly and annual time scales over global land and selected  
149 168 river basins to investigate the sensitivity of the ET-WB performance using various evaluation metrics, including Pearson



150 correlation coefficient (CC), Nash-Sutcliffe efficiency (NSE), root mean square error (RMSE), and relative bias (RB). They  
151 describe different aspects of ET-WB performance; for example, CC [-1,1] measures the linear correlation with auxiliary ET  
152 products, and NSE ( $\leq 1$ ) determines the relative magnitude of residuals between observations and predictions relative to the  
153 variance of the former. RMSE ( $\geq 0$ ) quantifies the differences between ET-WB and other existing ET products, while it is not  
154 normalized and challenging to compare basins with different ET amplitudes. As such, the metric RB (can be negative or  
155 positive) is used to express the relative bias of ET-WB compared with other ET datasets over the period. Mathematically, these  
156 metrics are defined as follows:

$$157 \quad CC = \frac{\sum(ET_G - \overline{ET}_G) \cdot (ET_{WB} - \overline{ET}_{WB})}{\sqrt{\sum(ET_G - \overline{ET}_G)^2} \cdot \sqrt{\sum(ET_{WB} - \overline{ET}_{WB})^2}} \quad (2)$$

$$158 \quad NSE = 1 - \frac{\sum(ET_G - ET_{WB})^2}{\sum(ET_G - \overline{ET}_G)^2} \quad (3)$$

$$159 \quad RMSE = \sqrt{\left(\frac{\sum(ET_G - ET_{WB})^2}{n}\right)} \quad (4)$$

$$160 \quad RB = \frac{\sum(ET_{WB} - ET_G)}{\sum ET_G} \cdot 100\% \quad (5)$$

161 where  $ET_G$  represents the auxiliary global ET products for comparison with the ET-WB, i.e.,  $ET_{WB}$  in Equations 2-5. Secondly,  
162 further comparisons were performed at the level of long-term mean and trend, which were calculated using Sen's slope method  
163 (Sen, 1968). Sen's slope method can overcome the impacts of outliers on time series and can be more accurate than the  
164 traditional linear regression, especially for the heteroskedastic time series (Sen, 1968). Different temporal coverage of the  
165 auxiliary global ET datasets is considered, so only consistent periods with the ET-WB are used for calculations.

### 166 2.3 Uncertainty estimation

167 Uncertainty in ET-WB and its contributing variables (e.g., P) is quantified using different methods. Specifically, we estimated  
168 the uncertainty in various TWSA datasets from GRACE solutions and GHM as the residual after removing the long-term trend,  
169 interannual signals, and seasonal cycles based on the Seasonal and Trend decomposition using Loess (STL) method (Cleveland  
170 et al., 1990). The STL method can robustly decompose the TWSA monthly time series into long-term, seasonal, and residual  
171 components, in which the long-term signal can be further separated as a long-term trend and the non-linear (interannual) signals  
172 (Cleveland et al., 1990; Scanlon et al., 2018; Vishwakarma et al., 2021) as:

$$173 \quad S_{total} = S_{long-term} + S_{seasonal} + S_{residual} \quad (6)$$

174 where  $S_{total}$  is the original TWSA time series,  $S_{long-term}$  is the long-term components of time series consisting of the long-  
175 term trend and the remaining interannual components,  $S_{seasonal}$  is the seasonal cycle time series of TWSA, and  $S_{residual}$  is  
176 the noise and/or other high-frequency (i.e., sub-seasonal) signals. Further, the uncertainty in  $\Delta S$  was computed from the



177 uncertainties in TWSA for back and forward months added in quadrature, followed by the determinations of the root mean  
178 squares (RMS) from different results (Long et al., 2014). However, a few studies also indicate that this method might  
179 overestimate the actual uncertainty as the residual temporal signals might contain real information (e.g., sub-seasonal signals)  
180 (Scanlon et al., 2018). For other water components, including P and R, we assumed the standard deviation (SD) across the  
181 ensemble as the uncertainties since we do not have the formal error budget for the multi-source global products from models,  
182 satellites, and field monitoring networks. Uncertainty in the auxiliary ET products used for comparison with ET-WB is also  
183 estimated using the SD method. It should be noted that the SD estimations may underestimate the actual uncertainty because  
184 of the inadequate number of datasets considered in our study. We took different strategies to estimate the uncertainty in  $\Delta S$   
185 and other variables because of the strong correlation of the selected GRACE solutions, which can lead to a very low SD among  
186 datasets. A similar situation can occur in R, where 23 out of 29 R datasets are from the G-RUN ensemble with similar  
187 algorithms (but with different meteorological forcing data). The SD of different auxiliary global ET products was also  
188 calculated for comparison, which can be written as:

$$189 \quad SD = \sqrt{\frac{\sum(X - \bar{X})^2}{n}} \quad (7)$$

190 where  $X$  is the hydrological time series of different variables. Thus, we could estimate the uncertainty in the ET-WB by  
191 propagating the above uncertainties in quadrature with the assumption of independence and normal distribution among  
192 different water fluxes (Rodell et al., 2004):

$$193 \quad U_{ET-WB} = \sqrt{\sum(U_P^2 + U_R^2 + U_{\Delta S}^2)^2} \quad (8)$$

194 where  $U_P$ ,  $U_R$ , and  $U_{\Delta S}$  are the estimated uncertainty for P, R, and  $\Delta S$  on the monthly scale, respectively. We utilized the RMS  
195 to represent the average uncertainty over the whole study period as:

$$196 \quad RMS = \sqrt{\left(\frac{\sum Y^2}{n}\right)} \quad (9)$$

197 where  $Y$  denotes the monthly estimates of uncertainty in different variables (e.g., ET-WB). The relationships between  
198 uncertainty in ET-WB and basin area, climate condition (aridity), and human activities (irrigation) are also detected to  
199 thoroughly investigate the influential factors on the performance of ET-WB.

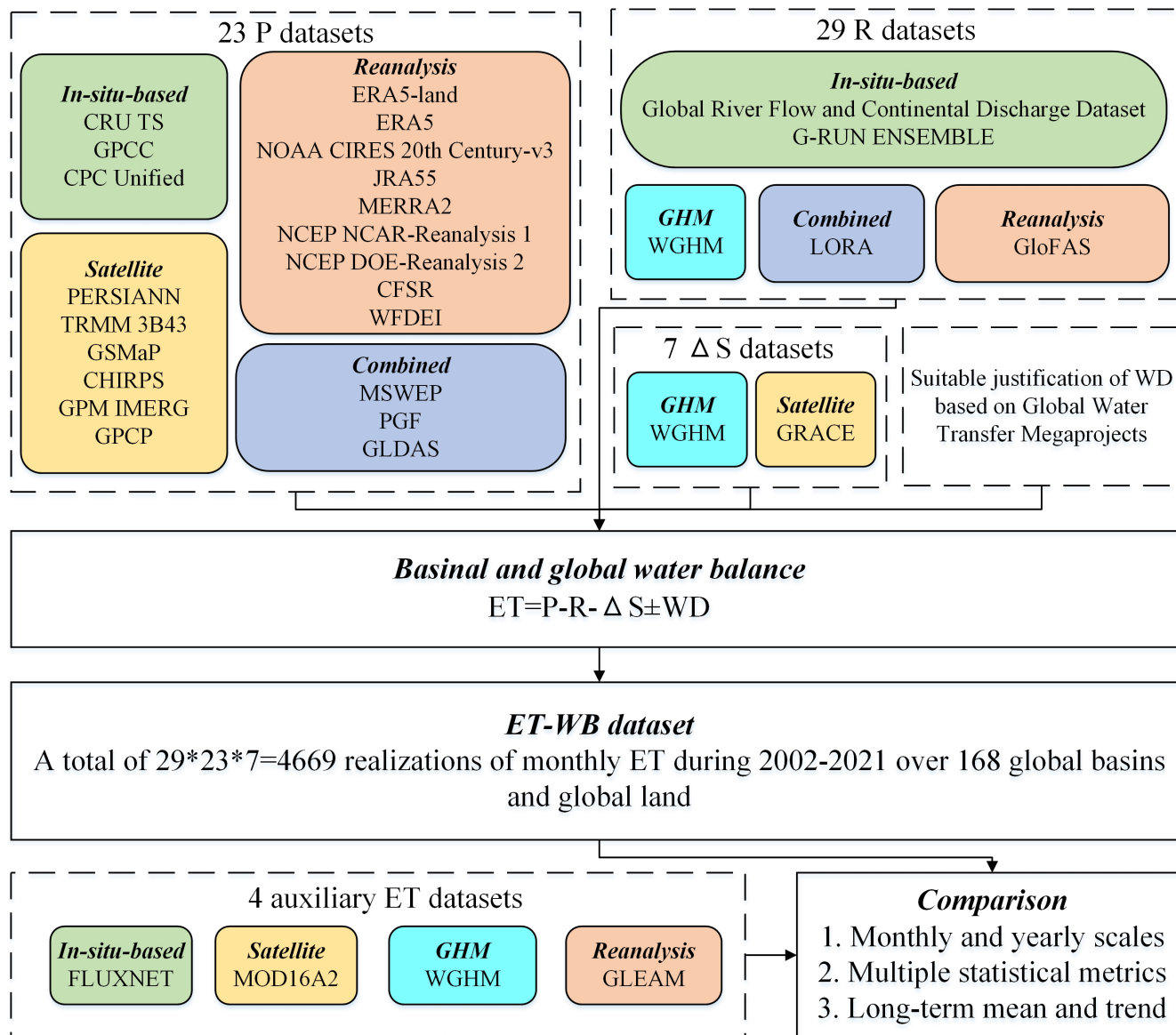
### 200 **3 Data**

201 Several criteria are applied to select the appropriate datasets for the development of ET-WB: (1) only the publicly available  
202 global datasets are chosen to increase the transparency and reproducibility of our study, (2) the temporal resolution should be  
203 equal to or smaller than one month, spanning at least from 2002 to 2014, (3) the spatial resolution should be finer than  $2^\circ$  to  
204 constrain the uncertainties over small river basins ( $\sim 64,000 \text{ km}^2$  for the minimum), and the spatial coverage should be



205 (quasi-)global to reach most river basins. Alternative factors like the frequency of data updates (mostly are near-real-time and  
206 a few are yearly), the recognition in the community (some datasets not being widely used were excluded), and the data types  
207 (try taking more categories of datasets into account, e.g., satellite, modeling, reanalysis, and in-situ-based products) are also  
208 considered. As such, we used 23 P, 29 R, and 7  $\Delta$ S datasets to generate a total of 4669 subsets of ET-WB during May 2002-  
209 December 2021 over 168 river basins and global land, excluding Greenland and Antarctica. We simultaneously selected the  
210 datasets belonging to the same series but with different versions, for example, GLDAS-v1/v2 and NCER/CFSR, because the  
211 older version (e.g., NCER/NCEP) is still updating, and the improvements of the newer version might not be significant and  
212 consistent over all the regions of the world (Qi et al., 2018, 2020). Despite this, it is acknowledged that it is impossible to  
213 consider all the existing datasets meeting the above inclusion criteria because the development of global datasets is advancing  
214 rapidly. All the selected datasets are provided on a grid cell scale and converted into basin-scale based on the changing area of  
215 grid cells over latitude. Hence the varying spatial resolutions of datasets do not require the up/down-scaling processes in our  
216 study. Moreover, most of the products are on a monthly time scale, consistent with the ET-WB estimations. A few daily  
217 datasets are aggregated into monthly time scales by taking the sum from the first to the last day of the certain month, which  
218 might cause some discrepancies with the GRACE solutions because the time sampling of GRACE products is not strictly  
219 distributed within a month (Tapley et al., 2004). As different datasets might have varying temporal and spatial coverage (Fig.  
220 2), the missing months in recent one or two years due to update latency, as well as the basins suffering from incomplete spatial  
221 coverage, are set as NA values. Please find detailed information on the datasets used in our study in Table 1. A more intuitive  
222 work chain for the generation of ET-WB and the related data processing flow is presented in Fig.2.

223



224  
 225  
 226  
 227

**Figure 2: Flowchart and the characteristics of the data sets in the study. Please see the data section for detailed descriptions of the various datasets.**

**Table 1. Datasets used in our study.**

Variable	Dataset	Type	Reference	Selected period	Temporal resolution	Spatial resolution (longitude×latitude)	Spatial coverage
----------	---------	------	-----------	-----------------	---------------------	---	------------------



	G-RUN Ensemble	In-situ based	Ghiggi et al., 2021	2002.5-2019.12	Monthly	0.5°×0.5°	Global land excluding Antarctica
	LORA-v1.0	Combined product	Hobeichi et al., 2019	2002.5-2012.12	Monthly	0.5°×0.5°	Global land excluding Greenland and Antarctica
	WGHM	GHM	Schmied et al., 2021	2002.5-2016.12	Monthly	0.5°×0.5°	Global land excluding Antarctica
Runoff	Global River Flow and Continental Discharge Dataset	In situ	Dai and Trenberth, 2002	2002.5-2018.12	Monthly	Gauge stations	Global major river basins
	GloFAS-v2.1	Reanalysis	Harrigan et al., 2020	2002.5-2021.12	Daily	0.1°×0.1°	Global land excluding Antarctica
	GloFAS-v3.0	Reanalysis	Alfieri et al., 2020	2002.5-2018.12	Daily	0.1°×0.1°	Global land excluding Antarctica
	GloFAS-v3.1	Reanalysis	Harrigan et al., 2020	2002.5-2021.12	Daily	0.1°×0.1°	Global land excluding Antarctica
	ERA5-land	Reanalysis	Muñoz-Sabater et al., 2021	2002.5-2021.12	Monthly	0.1°×0.1°	Global land
	ERA5	Reanalysis	Hersbach et al., 2020	2002.5-2021.12	Monthly	0.25°×0.25°	Global land and ocean
Precipitation	NOAA CIRES 20th Century-v3	Reanalysis	Slivinski et al., 2019	2002.5-2015.12	Monthly	0.702°×0.702°	Global land and ocean
	JRA55	Reanalysis	Kobayashi et al., 2015	2002.5-2021.12	Monthly	55 km×55 km	Global land and ocean
	MERRA2	Reanalysis	Gelaro et al., 2017	2002.5-2021.12	Monthly	0.625°×0.5°	Global land excluding Greenland and Antarctica
	NCEP NCAR-Reanalysis 1	Reanalysis	Kistler et al., 2001	2002.5-2021.12	Monthly	1.875°×1.9048°	Global land and ocean



NCEP DOE-Reanalysis 2	Reanalysis	Kanamitsu et al., 2002	2002.5-2021.12	Monthly	1.875°×1.9048°	Global land and ocean
CFSR-v1&2	Reanalysis	Saha et al., 2010	2002.5-2021.12	Monthly	0.5°×0.5°	Global land and ocean
WFDEI	Reanalysis	Weedon et al., 2014	2002.5-2016.12	Monthly	0.5°×0.5°	Global land excluding Antarctica
PERSIANN CDR-v1	Satellite	Ashouri et al., 2015	2002.5-2021.12	Daily	0.25°×0.25°	60° S–60°N
TRMM 3B43-v7	Satellite	Huffman et al., 2007	2002.5-2019.12	Monthly	0.25°×0.25°	50° S–50°N
GSMaP	Satellite	Okamoto et al., 2005	2002.5-2021.12	Monthly	0.1°×0.1°	60° S–60°N
CHIRPS-v2.0	Satellite	Funk et al., 2015	2002.5-2021.12	Daily	0.25°×0.25°	Global land between 50° S–50°N
GPM IMERG-v06	Satellite	Huffman et al., 2019	2002.5-2021.9	Monthly	0.1°×0.1°	60° S–60°N
GPCP-v3.2	Satellite	Huffman et al., 2022	2002.5-2020.12	Monthly	0.5°×0.5°	Global land and ocean
CRU TS-v4.06	In situ-based	Harris et al., 2020	2002.5-2021.12	Monthly	0.5°×0.5°	Global land excluding Antarctica
GPCC-v2020	In situ-based	Schneider et al., 2020	2002.5-2019.12	Monthly	0.25°×0.25°	Global land excluding Antarctica
CPC Unified	In situ-based	Chen and Xie, 2008	2002.5-2021.12	Daily	0.5°×0.5°	Global land
MSWEP-v2.8	Combined product	Beck et al., 2019	2002.5-2021.12	Monthly	0.1°×0.1°	Global land and ocean
PGF-v3	Combined product	Sheffield et al., 2006	2002.5-2016.12	Monthly	0.25°×0.25°	60° S–90°N
GLDAS-v1	Combined product	Rodell et al., 2004	2002.5-2019.6	Monthly	1°×1°	Global land excluding Antarctica



	GLDAS-v2.0	Combined product	Rodell et al., 2004	2002.5-2014.12	Monthly	1°×1°	Global land excluding Antarctica
	GLDAS-v2.1	Combined product	Rodell et al., 2004	2002.5-2021.12	Monthly	1°×1°	Global land excluding Antarctica
Actual evaporation	MODIS16	Satellite	Mu et al., 2011	2002.5-2014.12	Monthly	0.5°×0.5°	60° S–80°N
	FLUXCOM	In situ-based	Jung et al., 2019	2002.5-2015.12	Monthly	0.5°×0.5°	Global land excluding Antarctica
	GLEAM-v3.6a	Satellite	Martens et al., 2017	2002.5-2021.12	Monthly	0.25°×0.25°	Global land
	WGHM	GHM	Schmied et al., 2021	2002.5-2016.12	Monthly	0.5°×0.5°	Global land excluding Antarctica
Terrestrial water storage anomaly	GRACE CSR RL06 mascons-v02	Satellite	Save et al., 2016	2002.4-2021.12	Monthly	0.25°×0.25°	Global land and ocean
	GRACE JPL RL06 mascons-v02	Satellite	Wiese et al., 2018	2002.4-2021.12	Monthly	0.5°×0.5°	Global land and ocean
	GRACE GSFC RL06 mascons-v02	Satellite	Loomis et al., 2019	2002.4-2021.12	Monthly	0.5°×0.5°	Global land and ocean
	GRACE CSR RL06 Level-2 SH	Satellite	Swenson and Wahr, 2006	2002.4-2021.12	Monthly	1°×1°	Global land and ocean
	GRACE JPL RL06 Level-2 SH	Satellite	Swenson and Wahr, 2006	2002.4-2021.12	Monthly	1°×1°	Global land and ocean
	GRACE GFZ RL06 Level-2 SH	Satellite	Swenson and Wahr, 2006	2002.4-2021.12	Monthly	1°×1°	Global land and ocean
	WGHM	GHM	Schmied et al., 2021	2002.4-2016.12	Monthly	0.5°×0.5°	Global land excluding Antarctica



### 229 3.1 Precipitation

230 As summarized in Table 1, 23 precipitation data sets from different sources were used as input for the water balance equation  
231 (Eq. 1). Three global datasets based on in-situ observations are collected, including the Climatic Research Unit Time Series  
232 (CRU TS) database, the Global Precipitation Climatology Centre (GPCC) project, and the unified suite from NOAA Climate  
233 Prediction Center (CPC Unified). They generally rely on the point-scale collections of rain gauges worldwide to interpolate  
234 the gridded global products. Specifically, the CRU TS dataset incorporates more than 10,000 gauge stations to derive the  
235 monthly global gridded data since 1901 based on the angular-distance weighting method with an annual update (Harris et al.,  
236 2020). The GPCC project contains the quality-controlled gauge measurements from approximately 67,200 stations worldwide  
237 with at least 10 uninterrupted years of available data and then interpolates and superimposes them on the final gridded product  
238 in the corresponding resolution (Schneider et al., 2020). The CRU TS and GPCC datasets have almost identical temporal  
239 coverage and resolution and mainly rely on national meteorological agencies and related international institutions like WMO  
240 and FAO. The CPC Unified dataset is constructed from over 30,000 rain gauges from Global Telecommunication System  
241 (GTS), Cooperative Observer Network (COOP), and other national and international institutions. The daily analysis is released  
242 on multiple spatial resolutions over the global domain from 1979 to the present (Chen and Xie, 2008). The main advantages  
243 of these gauge-based global datasets stem from their large historical records dating back to the beginning of the 20<sup>th</sup> century,  
244 high accuracy, and effective construction cost. However, they heavily suffer from inhomogeneous spatial distribution and  
245 substantial maintenance efforts, especially in developing regions with complicated topography like North Africa and Qinghai-  
246 Tibetan Plateau. Therefore, the remote sensing technique has become a popular choice in learning global precipitation  
247 information in recent decades, which greatly improves precipitation measurement in ungauged and poorly gauged areas.

248 Six remote sensing products have been collected to enrich our study, namely the Integrated Multi-Satellite Retrievals  
249 (IMERG) for Global Precipitation Measurement (GPM), Global Precipitation Climatology Project (GPCP), Precipitation  
250 Estimation from Remotely Sensed Information using Artificial Neural Network-Climate Data Record (PERSIANN-CDR),  
251 Tropical Rainfall Measuring Mission with 3B43 algorithm (TRMM 3B43), Global Satellite Mapping of Precipitation (GSMaP),  
252 and Climate Hazards Group InfraRed Precipitation with Station data (CHIRPS). The TRMM 3B43 product algorithmically  
253 merges the microwave observations from multiple sensors, including precipitation radar and visible and infrared scanner (VIRS)  
254 loaded in the TRMM, which is a joint space satellite between NASA and Japan's National Space Development Agency to  
255 monitor tropical and subtropical precipitation from 1997 to 2015 (Huffman et al., 2007). Then, the successor GPM mission,  
256 an international network of satellites carrying the first space-borne Ku/Ka-band Dual-frequency Precipitation Radar (DPR)  
257 and a multi-channel GPM Microwave Imager (GMI), continued to provide the global precipitation data up to the present  
258 (Huffman et al., 2019). The IMERG algorithm can integrate all information from satellites constellation at a given time to  
259 estimate precipitation on the Earth's surface. The satellite observations in the TRMM era were also re-processed using the  
260 IMERG algorithm to create long-term continuous records, but the production stopped at the end of 2019. The GSMaP is a  
261 blended satellite-based precipitation dataset from the passive microwave sensors in low Earth orbit and infrared radiometers



262 in geostationary Earth orbit, which was developed by Japan Aerospace Exploration Agency (JAXA) and became the Japanese  
263 GPM standard product (Okamoto et al., 2005). The GSMaP product can distribute the global precipitation over the region from  
264 60° N to 60° S at a high spatial resolution of 0.1°×0.1°. In addition, the CHIRPS dataset, building on the ‘smart’ interpolation  
265 techniques and high resolution, long period of precipitation records from the infrared Cold Cloud Duration measurements, is  
266 developed by the USGS and Climate Hazards Group at the University of California. It has supplied precipitation estimates  
267 over global land within the range of 50° N to 50° S since 1981 (Funk et al., 2015). The PERSIANN product applies the trained  
268 artificial neural network on GridSat-B1 infrared satellite data of brightness temperature of cold cloud pixels to produce the  
269 rain rate estimates in the latitude band 60° S-60° N from 1983 to the (delayed) present (Ashouri et al., 2015). The GPCP  
270 precipitation dataset dynamically merges various satellite-based information, such as passive microwave and infrared data,  
271 along with the GPCC gauge measurements, contributing to the monthly precipitation estimates from 1979-present worldwide  
272 (Huffman et al., 2022). To control the systematic bias of the satellite sensors, bias correction based on gauge observations (e.g.,  
273 GPCC) and satellite observations (e.g., GPCP) is necessary, particularly over regions having poor gauge coverage, like Africa  
274 and the ocean.

275 Although the remote sensing technique is a robust option for global precipitation estimations, it still has some  
276 drawbacks, like the relatively short lifetime, the complexity of the retrieval algorithm, and the need for in-situ observations for  
277 bias correction. Thus, global reanalysis products that synthesize multiple geophysical and climatological data to produce high-  
278 resolution precipitation simulations have been developed. We obtained nine reanalysis datasets, including the fifth-generation  
279 reanalysis product of the European Centre for Medium-Range Weather Forecasts (ERA5), the land component of ERA5  
280 (ERA5-land), the Twentieth Century Reanalysis by NOAA, the University of Colorado Boulder’s Cooperative Institute for  
281 Research in Environmental Sciences, and the U.S. Department of Energy (NOAA CIRES 20th Century), the Japanese 55-year  
282 Reanalysis (JRA55), the Modern-Era Retrospective analysis for Research and Applications (MERRA), the Reanalysis I project  
283 from the National Centers for Environmental Prediction and the National Center for Atmospheric Research (NCEP NCAR-  
284 Reanalysis 1), the Reanalysis II project from the NCEP and DOE (NCEP DOE-Reanalysis 2), the NCEP Climate Forecast  
285 System Reanalysis (CFSR), and the WATCH Forcing Data methodology applied to ERA-Interim reanalysis data (WFDEI).  
286 The ERA5 reanalysis, as the latest global reanalysis following ERA-14, ERA-40, and ERA-Interim, provides a comprehensive  
287 field of the global atmosphere, land surface, and ocean waves by assimilating numerous historical observations (e.g., satellite  
288 precipitation data from microwave imagery and few gauge measurements) into the ECMWF Integrated Forecasting System  
289 (IFS) Cy41r2 (Hersbach et al., 2020). The ERA5 reanalysis can simulate the global precipitation with a sophisticated spatial  
290 and temporal resolution with a total of 137 mode layers of 0.01 hPa from 1959 to near real-time. ERA5-land is a re-run of the  
291 land component of ERA5, which is designed to provide a consistent view of land variables over several decades, but with an  
292 enhanced resolution than ERA5 (Muñoz-Sabater et al., 2021). The WFDEI meteorological forcing dataset, however, is  
293 generated based on the ERA-Interim reanalysis after bias correction from gridded observations (i.e., GPCC) and sequential  
294 elevation correction (Weedon et al., 2014). Several classic reanalyses from NCEP are used in our study. NCEP NCAR-  
295 Reanalysis 1 project uses a state-of-the-art forecast system to perform data assimilation during the period 1948-now, while



296 with a relatively coarse spatial resolution of  $\sim 2^\circ$ , which might cause some errors in small basins upon calculation of basin-  
297 average precipitation (Kistler et al., 2001). We note the precipitation observations are not assimilated into the assimilation  
298 system, so the precipitation from the reanalysis are short-range model forecast accumulations (Janowiak et al., 1998). The  
299 NCEP DOE-Reanalysis 2 is an improved version of the NCEP NCAR-Reanalysis 1, including an updated model with more  
300 realistic physical parameterizations, fixed data assimilation errors, and more digested data (Kanamitsu et al., 2002). The NCEP  
301 DOE-Reanalysis 2 replaces the model precipitation at the land surface with observed data from NCEP/CPC global precipitation  
302 analysis that merges satellite and gauge measurements (Xie and Arkin, 1997). Furthermore, as an important update from NCEP,  
303 the CFSR uses a high-resolution model that is fully coupled with the atmospheric component at a resolution of 38 km with 64  
304 vertical levels from the land surface to 0.26 hPa between 1979 and the present (Saha et al. 2010). Similarly, the CFSR reanalysis  
305 applies the CMAP (Xie and Arkin, 1997) and CPC unified precipitation analysis to reduce the bias derived from the modeled  
306 precipitation in the initial version of NCEP NCAR-Reanalysis 1. Given most analyses only focus on the Earth's status in the  
307 recent half-century, the NOAA CIRES 20th Century project is the first ensemble of sub-daily global atmospheric conditions  
308 spanning over 100 years from 1836 to 2015, providing the best estimate of the weather at any place and time based on the  
309 upgraded data assimilation method, higher resolution, and larger datasets of observations than the previous versions (Slivinski  
310 et al., 2019). We note the NOAA CIRES 20th Century did not incorporate any precipitation observations, meaning the  
311 reanalysis of precipitation is only from the predictions of models. Since the reanalysis provides 80 ensemble members to  
312 constrain the uncertainty fully, we take the ensemble mean as the final precipitation estimate. The JRA55 reanalysis, managed  
313 by Japan Meteorological Agency (JMA), also derives precipitation from remote sensing products combining the model forecasts  
314 since 1958, attempting to provide comprehensive fields of atmosphere to foster the applications in multidecadal variability and  
315 climate change (Kobayashi et al., 2015). The MERRA 2 analysis from the NASA Global Modeling and Assimilation Office  
316 using the GEOS-5.12.4 system covers the period from 1980 to the present with a latency of weeks, with the output resolution  
317 of  $0.5^\circ(\text{latitude}) \times 0.625^\circ(\text{longitude})$ . The precipitation from MERRA2 reanalysis follows the assimilation strategy of CFSR,  
318 i.e., consider the CMAP and CPC Unified from NOAA CPC for assimilation. The quality of MERRA2 precipitation has been  
319 evaluated in a previous study, and relatively bad accuracy in high latitudes was reported (Reichle et al., 2017).

320 We also consider several 'combined products' that merge the above-mentioned data sources, including gauges,  
321 satellites, and reanalysis to estimate precipitation, including the Multi-Source Weighted-Ensemble Precipitation (MSWEP),  
322 Princeton Global Forcings (PGF), and different versions of Global Land Data Assimilation System (GLDAS). The MSWEP  
323 dataset that is featured by full global coverage, high spatial ( $0.1^\circ$ ) and temporal (3-hourly) resolutions, and distributional bias  
324 corrections optimally merges the precipitation records from gauge measurements (e.g., GPCC), satellite solutions (e.g.,  
325 TRMM), and reanalysis (e.g., JRA55) and achieve better performance than each of the members during the period 1979-now  
326 (Beck et al., 2019). The global and long-term PGF forcing dataset is constructed using the NCEO NCAR-Reanalysis 1 and  
327 multiple observation-based precipitation datasets such as TRMM, GPCP, and CRU TS products to perform the temporal and  
328 spatial downscaling, contributing to the high-resolution precipitation estimations from 1948 to 2016. The GLDAS forcing  
329 dataset generally applies precipitation of different types in different eras. Specifically, GLDAS (v1.0) switches from ECMWF



330 reanalysis during 1979-1993 to NCEP NCAR-Reanalysis 1 during 1994-1999 and finally uses the CMAP fields from 2001 to  
331 2019 with the NOAA/GDAS atmospheric applied in the year 2000 (Wang et al., 2016). However, the GLDAS (v2.0)  
332 precipitation is from the PGF dataset as the only source from 1948 to 2014. Differently, the GLDAS (v2.1) simulations are  
333 forced with a combination of GDAS, disaggregated daily GPCP precipitation, and AFWA radiation datasets from 2000 to the  
334 present. Please find detailed information about the product version and spatial/temporal resolution in Table 1.

### 335 3.2 Runoff

336 Similar to the precipitation, we also collected R datasets from different sources to feed the water balance equation. Firstly, we  
337 collected in-situ discharge measured at the mouths of the rivers from the dataset provided by Dai and Trenberth (2002), namely  
338 the Global River Flow and Continental Discharge Dataset. This observational dataset was compiled from many sources,  
339 including Bodo (2001), NCAR archive, and R-ArcticNET dataset (<http://www.R-ArcticNET.sr.unh.edu>), and has undergone  
340 the data quality controls during the compilation to avoid errata and inconsistencies. It contains monthly mean volume  
341 observations in 925 major rivers of the world since the 1900s (different rivers have varying lengths) and updates at an irregular  
342 time step (last updated in May 2019). The estimate of global continental freshwater discharge based on the dataset compares  
343 well with alternative estimates and ECMWF reanalysis, though there are some differences among the discharge into the  
344 individual ocean basins. The water volume is converted into the equivalent water depth by dividing the drainage area of the  
345 station. About one-third of the selected 168 river basins are included in this observational dataset, and the missing months  
346 without observation (e.g., after 2019) are set as NA values in the water balance calculation. Apart from this, most of the runoff  
347 datasets used in our study are from a global runoff reconstruction, named Global RUNoff ENSEMBLE (G-RUN ENSEMBLE),  
348 which provides a global runoff reanalysis of monthly runoff rates covering decades to the recent century at a resolution of  $0.5^\circ$   
349 (Ghiggi et al., 2021). The observation-based G-RUN ENSEMBLE employs the random forest method to learn the runoff  
350 generation using the gridded meteorological observations (precipitation and temperature) with the calibration of the Global  
351 Streamflow Indices and Metadata Archive (GSIM) (Do et al., 2018). The most significant improvement of G-RUN  
352 ENSEMBLE compared to its previous version (GRUN, Ghiggi et al., 2019) is that it considers the forcing uncertainty by  
353 deriving a total of 23 subsets from multiple meteorological reanalysis and observations. Although one of the 23 G-RUN  
354 ENSEMBLE members forced by WATER and global CHange (WATCH) Forcing Data (WFD) only provides the global runoff  
355 data up to December 2001, we still keep it in our study for consistency. It would not influence the water balance estimations  
356 of ET-WB as all the missing months are taken as NA values during calculation. We note an implicit assumption in the  
357 generation of G-RUN ENSEMBLE is that the storage of river water loss can be minimal so the monthly river discharge of the  
358 river mouth equals the average catchment runoff depth. Given that the G-RUN ENSEMBLE is only calibrated from small  
359 catchments with areas ranging from 10 to 2,500 km<sup>2</sup>, this assumption might not be strictly valid for large river basins, although  
360 it has shown comparable performance with several global runoff simulations and reconstructions like the Global Drought and  
361 Flood Catalog (GDFC) (He et al., 2020) and ERA5. Moreover, the human activities, including human water use and reservoir  
362 management, lack a physical-based representation in the random forest machine learning method (but implicitly considered



363 during the model training), and the apparent outliers caused by human activities (e.g., an abrupt decrease of river discharge  
364 after dam construction) have been removed. Therefore, we additionally compare the R datasets used in our study (mainly from  
365 G-RUN ENSEMBLE) with the streamflow records from the GRDC archive in 53 river basins worldwide since they are the  
366 only regions where the discharge observations are available with the spatial and temporal consistency of our study (Table S3).  
367 A satisfactory performance of the estimations in the levels of multi-mean and long-term trends is found, which are the focus  
368 of our study and the relevant future applications (Fig. S1). We also used a synthesized global gridded runoff product that  
369 merges runoff estimates from different global hydrological models (GHM) constrained by hydrological observations using an  
370 optimal weighting method during 1980-2012 (namely Linear Optimal Runoff Aggregate, LORA), which works dynamically  
371 based on the comparisons with in-situ data when accounting for the variance among members (Hobeichi et al., 2019). The  
372 LORA product, with a consistent spatial resolution of  $0.5^\circ$ , is also used as the benchmarking dataset for G-RUN ENSEMBLE  
373 and achieved similar performance. A similar limitation is shared in these global gridded runoff reconstructions, i.e., the  
374 neglect of river routing, which may lead to an overestimation in the computed uncertainties over large basins. In addition,  
375 since the LORA is the merged result from eight GHMs with different physical structures and model parameterization schemes,  
376 the representation of the basins with significant anthropogenic activities should be taken with caution. For example, there is a  
377 low observed runoff of  $\sim 0$  across the regions having high irrigation areas and/or artificial surfaces. As an important member  
378 of the LORA dataset, the WaterGAP Global Hydrology Model (WGHM), providing the global water resources dynamics from  
379 1901-2016 at a  $0.5^\circ$  resolution (Müller Schmied et al., 2021), is also selected in our study for the computation of ET-WB. The  
380 most recent version (2.2d) of the WaterGAP framework consists of five water use models, including irrigation, livestock,  
381 domestic, manufacturing, and thermal power sections, the linking model that computes net abstractions from groundwater and  
382 surface water, and the WaterGAP Global Hydrology Model (Müller Schmied et al., 2021). The discharge simulations are  
383 applied in the water balance calculation, which was forced by WFDEI precipitation during the study period and considered the  
384 human effects such as dam management. The river routing schemes follow Döll et al. (2014), where water is routed through  
385 the storages depending on the fraction of surface water bodies. The state-of-the-art global river discharge reanalysis, the Global  
386 Flood Awareness System (GloFAS), serves as a significant supplement to the R inputs in water balance. The GloFAS system  
387 simulates the global discharge by coupling runoff simulations from the specific model forced with the ERA5 reanalysis and a  
388 channel routing model. The GloFAS product aims to provide daily high-resolution ( $0.1^\circ$ ) gridded river discharge forecasts  
389 from 1979 to near real-time. Different versions of GloFAS reanalysis are used in our study, where the main differences are  
390 from the hydrological modeling scheme. For example, the GloFAS (version-2.1) applies a combination of the Hydrology Tiled  
391 ECMWF Scheme for Surface Exchanges over Land (HTESSEL) land surface model with the LISFLOOD hydrological and  
392 channel routing model (Harrigan et al., 2019). The surface and subsurface runoff from the HTESSEL are used as input for the  
393 LISFLOOD model (Hirpa et al., 2018). For the newer versions like 3.0 and 3.1, both the runoff generation and routing  
394 processes are based on the full configuration of the LISFLOOD model, the former of which is an offline version provided by  
395 Alfieri et al. (2020), and the latter is an operational online version that was released in early 2020 with some changes in web  
396 and data services. Despite this, we take both into consideration as they are the only datasets providing near-real-time discharge



397 information. All the versions of GloFAS used in our study have been calibrated by more than 1,200 gauge stations worldwide,  
398 which greatly improves the performance than those without any calibrations (Alfieri et al., 2020). Some procedures are needed  
399 for discharge-type R datasets (i.e., WGHM and GloFAS-family products) to find the grid cell coinciding with the river mouth  
400 of the basin. For example, we find the certain grid with the maximum drainage area within the basin based on the static total  
401 upstream area file provided by GloFAS, which is defined as the catchment area for each river segment (i.e., the total area that  
402 contributes to water to the river at the specific grid point). Then, the discharge forecast of that grid point should be divided by  
403 the corresponding drainage area to be converted into equivalent water depth. For the global land, the total freshwater flowing  
404 into the ocean is estimated as the sum of the discharge of all the coastal grid cells based on a mask at the corresponding  
405 resolution (e.g.,  $0.1^\circ$  for GloFAS). As such, the differences in the spatial resolution (e.g.,  $0.5^\circ$  for the WGHM and  $0.1^\circ$  for the  
406 GloFAS) can contribute to some discrepancies in the final estimates of R. Finally, it is worth mentioning that we manually set  
407 the R-value as zero for the 13 endorheic basins without runoff flowing into the ocean, except for Volga, Ural, and Kura River  
408 basins that flow into the Caspian Sea (Fig. 1 and Table S2).

### 409 3.3 Terrestrial water storage

410 Seven global terrestrial water storage datasets are used to derive  $\Delta S$  and input the water balance equation. Six of these TWS  
411 datasets are GRACE solutions and one is from the WGHM. The GRACE mission has been the preferable tool to assess the  
412 large-scale variations in terrestrial water storage at a near-monthly scale from 2002 to 2017, with the GRACE Follow-On  
413 successor satellite launched in 2018 (Tapley et al., 2004; Kornfeld et al., 2019). There are generally two classes of methods to  
414 retrieve TWS anomaly signals from GRACE measurements, the spherical harmonic (SH) and the mass concentration blocks  
415 (mascon) methods. The SH method is a standard for the first decade of the GRACE era, which is processed by parameterizing  
416 the global time-varying gravity field using SH coefficients (Wahr et al., 1998). However, such a method should undergo a  
417 series of post-processing of the truncation of degree/order in SH coefficients, spatial smoothing, de-correlation filtering, and  
418 replacement of low-degree coefficients, etc. Various background models, such as glacial isostatic adjustment and de-aliasing,  
419 should also be considered. Therefore, different methods have been developed to restore the signal leakage and bias introduced  
420 during the post-processing. These methods include additive and multiplicative approaches, model-based scaling factors, data-  
421 driven methods, and constrained and unconstrained forward modeling methods (Long et al., 2015; Chen et al., 2019;  
422 Vishwakarma et al., 2017). However, the mascon method has provided another user-friendly option for the community in  
423 recent years, which functions by parameterizing the Earth's gravity field with the regional mass concentration functions. This  
424 kind of method does not need substantial post-processing techniques for signal restoration and can attenuate the noise during  
425 the gravity inversion process through regularization of the solution (Save et al., 2016; Xiong et al., 2022a). So the increasing  
426 attention in the non-geophysical community has been attracted by the mascon solution over the years (Abhishek et al., 2021).  
427 However, it is noticed that different GRACE ground system institutions can perform the post-processing for the fundamental  
428 level-1 GRACE data using different strategies, for example, the varying algorithms to the effect of glacial isostatic adjustment  
429 and the regularization or stabilization of the regional mass concentration functions may affect the hydrological analysis at



430 smaller scales ( $< \sim 3^\circ$ ) (Scanlon et al., 2018; Watkins et al., 2015; Vishwakarma, 2020). In this case, we collected the latest  
431 Release Version 06 level-2 SH solutions from different official GRACE processing agencies, including the University of Texas  
432 Center for Space Research (CSR), NASA's Jet Propulsion Laboratory (JPL), and GeoforschungsZentrum Potsdam (GFZ), as  
433 well as three level-3 mascon solutions from CSR, JPL, and NASA's Goddard Space Flight Center (GSFC) during the period  
434 April 2002-December 2021, which is the longest time span that GRACE (and GRACE Follow-On) can achieve at the present  
435 stage. The signal leakage and bias in three SH solutions are corrected using the forward modeling method, with the above-  
436 mentioned standard processing procedures performed (Swenson and Wahr, 2006). The mascon JPL solution that employs a  
437 Coastal Resolution Improvement (CRI) filter that reduces signal leakage errors across coastlines has undergone the adjustment  
438 from official scaling factors based on the CLM land surface model (LSM) (Wiese et al., 2016). As previously mentioned at  
439 the beginning of the Data section, the inconsistent spatial resolution of different mascon solutions will not impact the ET-WB  
440 calculations as we only perform the water balance budget at the basin (and global) scale (Save et al., 2016; Loomis et al., 2019).  
441 The 33 missing months due to the data gap between two generations of GRACE missions and instrumental issues have been  
442 statistically interpolated using a recently proposed method based on the Singular Spectrum Analysis method (Yi and Sneeuw,  
443 2021). This method can infer missing data from long-term and oscillatory changes extracted from available observations and  
444 does not rely on any external forcing, thus avoiding the uncertainty introduced by other datasets (e.g., precipitation).

445         Apart from the GRACE solutions, the simulations from the WGHM model are also used to avoid the strong correlation  
446 among GRACE solutions and provide a potential alternative viewpoint. The WGHM simulations of TWS include most of the  
447 key components in the land system, including canopy, snow and ice, soil moisture, groundwater, and surface water bodies  
448 (e.g., river, lake, wetlands, and reservoirs). However, the glacier water storage is not simulated in WGHM, which might induce  
449 some errors in high-latitude cold regions (Müller Schmied et al., 2021). The major human interventions such as dam  
450 management and human water use are also considered, which have been reported to greatly impact the regional terrestrial  
451 water storage balance (Rodell et al., 2009). This is the main advantage of the selected WGHM over other widely used  
452 GHMs/LSMs, such as GLDAS VIC and Noah models. GRACE solutions generally provide the anomalies of TWS relative to  
453 a long-term mean, but the WGHM simulates the actual value of TWS. However, this will not affect our derivation for the  $\Delta S$   
454 and the subsequent ET-WB estimations.

### 455 **3.4 Evaporation**

456 Benchmarking ET-WB against other global ET products is crucial to evaluate its performance. With the principle of 'different  
457 types of datasets have their unique values' in mind, four different categories of auxiliary ET products have been chosen for  
458 comparison with ET-WB at multiple time and space scales. These include the MODIS Global Evapotranspiration Project  
459 (MOD16A2), the FLUXCOM ensemble dataset, the Global Land Evaporation Amsterdam Model (GLEAM), and the  
460 simulations from WGHM. The MOD16A2 product estimates the terrestrial ET as the sum of evaporation from soil and canopy  
461 layer and the transpiration from plant leaves and stems (Mu et al., 2011). This satellite-based dataset is estimated under the  
462 framework of the Penman-Monteith equation with the effective surface resistance to the evaporation from the land surface and



463 transpiration from plant canopy, which is estimated based on the MODIS remotely sensed data including surface albedo, land  
464 cover classification, and vegetation information. The MOD16A2 dataset was originally produced at a spatial resolution of 1km  
465 and a temporal resolution of 8-day from 2000-2014. However, we used the re-processed monthly 0.5° product provided by the  
466 Numerical Terradynamic Simulation Group (NTSG) at the University of Montana  
467 ([http://files.ntsg.umt.edu/data/NTSG\\_Products/MOD16/](http://files.ntsg.umt.edu/data/NTSG_Products/MOD16/)). The FLUXCOM “remote-sensing” database (“RS” setup) employs  
468 nine machine learning algorithms to integrate ~20,000 flux observations across the globe with the satellite-based predictors  
469 from the MODIS mission (Jung et al., 2019). Therefore, it is considered an observation-driven product of three energy balance  
470 variables, namely, net radiation, latent energy, and sensible heat. Nonetheless, the product is subject to uncertainty in the choice  
471 of prediction models and is also limited in spatial/temporal resolution (0.0833°/8-daily) and time coverage (2001-2015) of the  
472 satellite inputs. Similarly, we used the re-processed monthly version of the product with a resolution of 0.5° by spatial and  
473 temporal aggregation, which is the median value of the ensemble members per grid cell and month. A key difference between  
474 the FLUXCOM and other ET datasets is that the former focuses only on the vegetated region because of the lack of eddy tower  
475 observations in these regions, meaning the ET values in unvegetated (barren, permanent snow or ice, water) area was omitted.  
476 We convert the latent energy data to ET by dividing it with the latent heat of vaporization, a constant value of 2.45 MJ/kg (or  
477 multiplying 0.408 kg/MJ) or 28.35 W/m<sup>2</sup>. We note the FLUXCOM database also develops the “RS+METEO” setup that uses  
478 daily meteorological data and mean seasonal cycles of satellite data with three machine-learning approaches. Since the  
479 differences between these two setups over global basins are still unclear, and beyond the scope of our study, only the “RS”  
480 setup is chosen for comparison and demonstration with ET-WB. It needs to be mentioned that we did not use the in-situ  
481 measurements from the regional FLUXNET eddy covariance towers because of the uneven and sparse distribution from a  
482 global perspective, which is not consistent with the spatial scale of ET-WB. In addition, the GLEAM model estimates the  
483 terrestrial ET separately, which comprises the individual components of transpiration, interception loss, bare soil evaporation,  
484 snow sublimation, and open-water evaporation (Martens et al., 2017). It firstly estimates the potential ET using the Priestley-  
485 Taylor equation based on satellite observations of surface net radiation and near-surface air temperature, then converts the  
486 potential ET to actual ET using the evaporative stress factor, which is estimated from the remote sensing vegetation microwave  
487 vegetation optical depth and predicted root-zone soil moisture from a water balance model. The GLEAM is more inclined to  
488 a ‘reanalysis’ dataset as it does not use the satellite observations directly (like MOD16A2) but indirectly includes the satellite  
489 observations to estimate ET. Similar to the FLUXCOM dataset, the GLEAM product also has two sub-versions, ‘a’ and ‘b’,  
490 with the main difference in the time span (1981-2021 for ‘a’ and 2003-2021 for ‘b’) due to different inputs considered. We  
491 choose version 3.6a to compare with ET-WB. Finally, the hydrological simulations of ET from WGHM are also included for  
492 data consistency, which was previously used to contribute to the runoff, terrestrial water storage, and precipitation (WFDEI  
493 forcing) estimations. Moreover, an alternative source (GHM) of ET can also strengthen the justification upon the comparison  
494 with derived ET-WB.



## 495 4 Results

### 496 4.1 Global evaluation of ET-WB

#### 497 4.1.1 Monthly assessment

498 Comparison and analyses of ET-WB and auxiliary ET datasets are carried out at various temporal scales to examine the  
499 reliability of ET-WB comprehensively. The long-term average seasonal cycle of ET during the period 2002-2021 is detected  
500 over global land (Fig. 3a). A clear unimodal distribution is observed with the highest ET in July (median value: 65.61  
501 mm/month (mm/m)) and the lowest result in January (median value: 36.11 mm/m) based on ET-WB, with the spread range of  
502 roughly  $\pm 10$  mm/m from different subsets of the ensemble. Furthermore, the seasonal cycle of other ET products is generally  
503 within the range of ET-WB ensemble with similar intra-annual characteristics. All of the GLEAM, MODIS, and WGHM data  
504 illustrate an overestimation of ET from March to June and an underestimation between September and November compared  
505 with the median values of ET-WB, but they are completely within the range of the ET-WB ensemble. Nevertheless, the  
506 FLUXCOM product tends to have higher ET than ET-WB due to the fact that FLUXCOM only considers the ET in the  
507 vegetated regions, and the unvegetated areas, such as those in the deserts of Sahara and Qinghai-Tibetan Plateau are masked  
508 (Jung et al., 2019). This would subsequently influence our comparisons in basins with a certain proportion of unvegetated area  
509 and the global land.

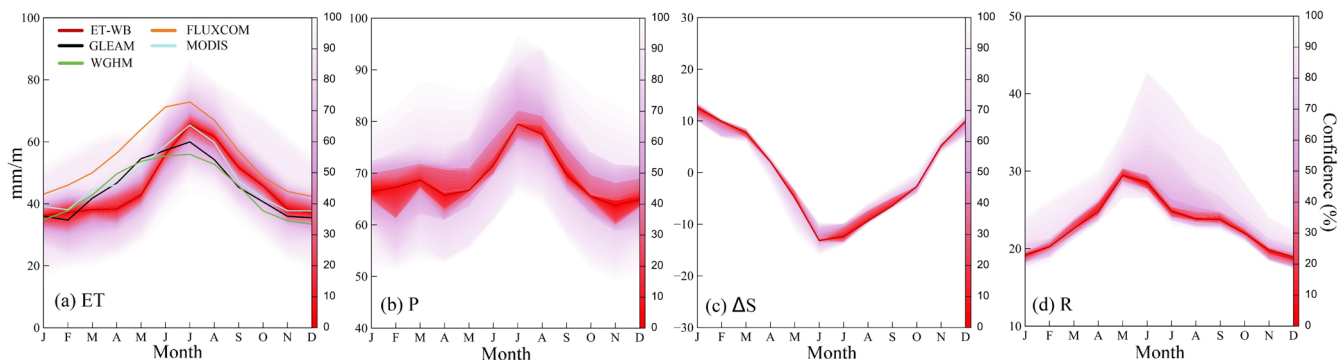
510 The seasonal pattern of ET-WB is highly consistent with that of precipitation in both amplitude and periodicity, which  
511 generally increase from the beginning to the middle of a year, followed by a gradual decrease. This contemporaneous relation  
512 between ET and P without time lag is also revealed by Rodell et al. (2015). However, the spread range in P is wider than ET-  
513 WB, meaning it is an important contributor to the uncertainty of the ET-WB, especially in water-limited months like February,  
514 April, and November (Fig. 3b). In addition, we also found that the seasonal cycle of  $\Delta S$  presents a reverse distribution than  
515 other water components (e.g., P and R), in which  $\Delta S$  decreases from positive to negative in the first half of the year (January  
516 to June) and then slowly rebound until the end of the year. In other words, the land system is losing water from April to October  
517 and gaining water until April of next year, implying a significant time lag between terrestrial water storage and P on a global  
518 scale (Fig. 3c). The narrow spread range of  $\Delta S$  is attributed to the high agreement between the six GRACE solutions used, not  
519 showing the real uncertainty of TWSA ( $\Delta S$ ) estimates. Counterintuitively, P lags R by two months, possibly related to the  
520 snowpack immobilization and the strength of summer convective rainfall in high-latitude regions (Rodell et al., 2015).  
521 Additionally, R demonstrates an interesting distribution with a constrained change range in all months with a few  
522 overestimations. It should be stemming from the reduced uncertainty in the choice of R datasets because we used the 23 (out  
523 of 29) G-RUN ENSEMBLE subsets that were generated using the same model but forced by different forcing, together with  
524 the interventions from other datasets (e.g., GloFAS reanalysis) (Fig. 3d).

525 Multiple statistical metrics are used to quantify the relative performance of the ET-WB product, which are calculated  
526 using the ensemble median ET and other global ET datasets. Global examinations of the relative bias (RB) based on different  
527 auxiliary datasets on the monthly scale indicate an overall agreement with ET-WB, with most (74%, 63%, 57%, and 77% for



528 GLEAM, FLUXCOM, MODIS, and WGHM, respectively) river basins having RB between -20% and 20% (Fig. 4). For the  
529 global land, the RB reaches 1.22%, -17.31%, -3.68%, and 2.96% for above four products, correspondingly, but with strong  
530 spatial heterogeneity among basins. Specifically, widespread overestimation of ET-WB than other datasets are reported in East  
531 Europe, West Russia, South and East Asia, and West Australia, with the maximum RB of nearly 300% in the Ashburton River  
532 basin (ID: 138) of Australia based on the MODIS ET dataset. On the contrary, the consistent underestimation of ET-WB  
533 compared with other products is also seen in West Europe, East Russia, and Southeastern basins of Australia, where RB is  
534 mostly small. However, divergent patterns of different ET datasets in parts of South and North America, Africa, and Central  
535 Asia highlight inherent uncertainty in each product and that it is impossible to have a single best-performing ET dataset for  
536 the whole globe. However, the RB values of ET-WB are within the range of  $\pm 20\%$ , meaning the ET-WB is comparable to  
537 these ET products and, therefore, can serve as an independent benchmarking product (Figs. 4a, 4c, 4e, and 4g). Alternative  
538 metrics like CC and NSE provide additional insights. Relatively better performance of ET-WB is apparent in the humid basins  
539 of high-latitude Eurasia, North America, and South China according to the comparably higher CC ( $>0.8$ ) and NSE ( $>0.4$ ) than  
540 other regions like South America and Africa (Figs. S2 and S3). This might be due to better simulation accuracy of, for example,  
541 reanalysis and GHMs, in humid zones than in arid regions. Though the reported NSE value may not appeal as satisfactory in  
542 an absolute sense, it only represents the median ET-WB. Distinctive choice of ET subset over different regions may lead to  
543 improved results, albeit without informing the full spread of the uncertainties. Additionally, RMSE results further convey  
544 higher errors of ET-WB in smaller regions than in larger ones (Fig. S4) because of the reduced retrieval errors of GRACE  
545 solutions as the basin size increases (Scanlon et al., 2018). The notable exception is the Amazon River basin (ID:1), which  
546 shows inconsistency between ET-WB and different ancillary products (e.g., GLEAM and MODIS). It is similar to a recent  
547 regional study (Baker et al., 2021), although a strong agreement between water balance ET and shortwave radiation was  
548 observed. For all the 168 basins, the scatter plots illustrate a reasonable agreement between ET-WB and multiple ET datasets  
549 (Figs. 4b, 4d, 4f, 4h). Despite the very small RB (from 0.09% of WGHM to -7.96% of MODIS), the skewed estimates are  
550 discovered in high-ET periods and regions, while most points having small ET values are perfectly located around the 1:1 line.  
551 Another discrepancy between ET-WB and other datasets is the existence of negative values of the former primarily in high-  
552 ET regions/periods, which is very likely resulting from the non-closure error among various water balance datasets (Pan et al.,  
553 2017; Rodell et al., 2011; Lehman et al., 2022) along with their respective shortcomings (e.g., non-consideration of river  
554 routing in G-RUN Ensemble runoff data) and should be delved into in future studies.

555  
556

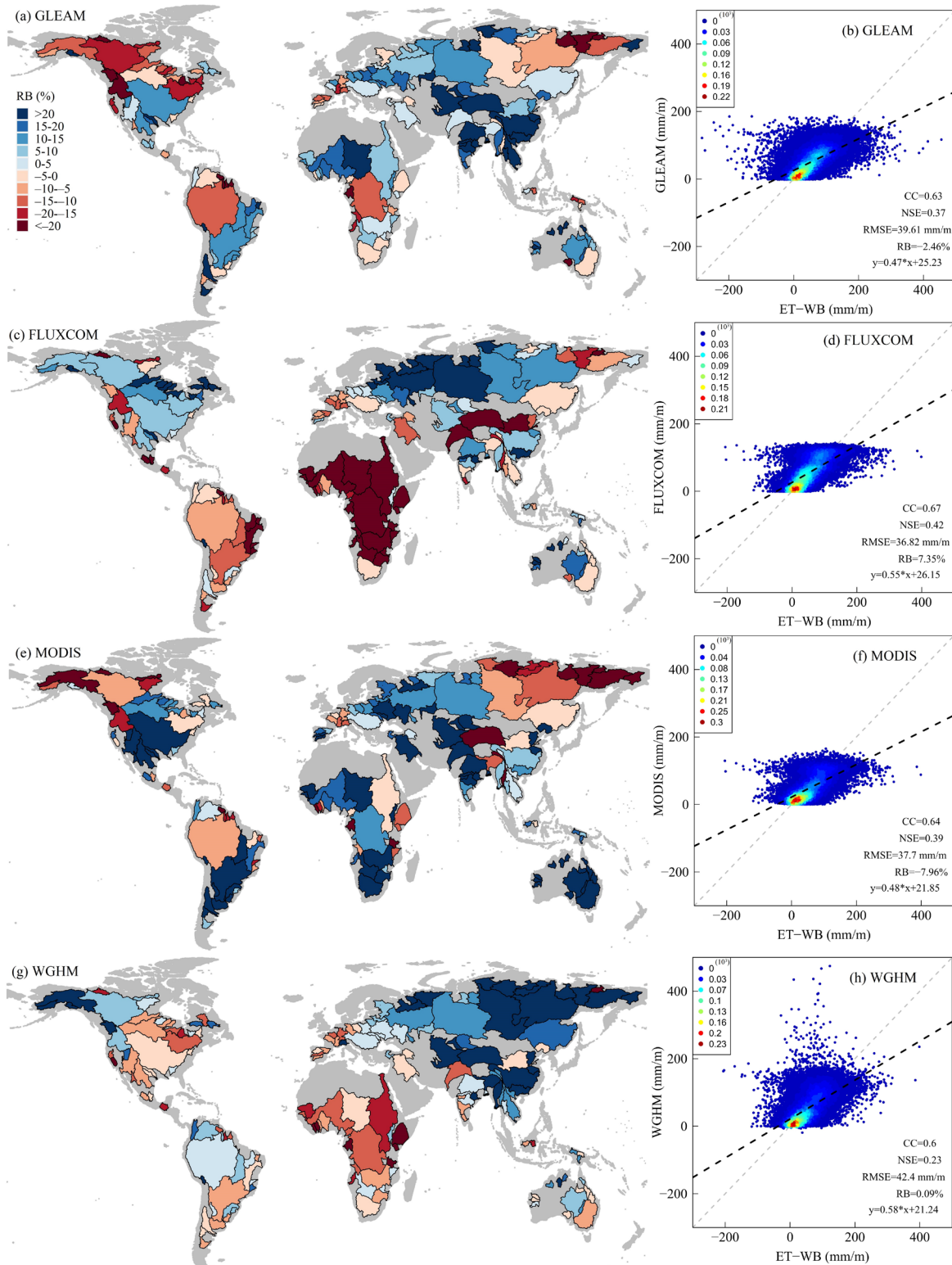


557

558

559

**Figure 3: Monthly average values of the ET-WB and multiple auxiliary ET products as well as other water components over global land during the period 2002-2021. The shading shows the spread range among different datasets.**





561 **Figure 4: Comparisons between the ET-WB and multiple auxiliary ET products (a, b: GLEAM; c, d: FLUXCOM; e, f: MODIS; g,**  
562 **h: WGHM) on a monthly scale during the period 2002-2021. The left column represents the global distribution of RB, and the right**  
563 **column represents the corresponding scatter plots. The color of the scatter points indicates the kernel density.**

#### 564 4.1.2 Annual assessment

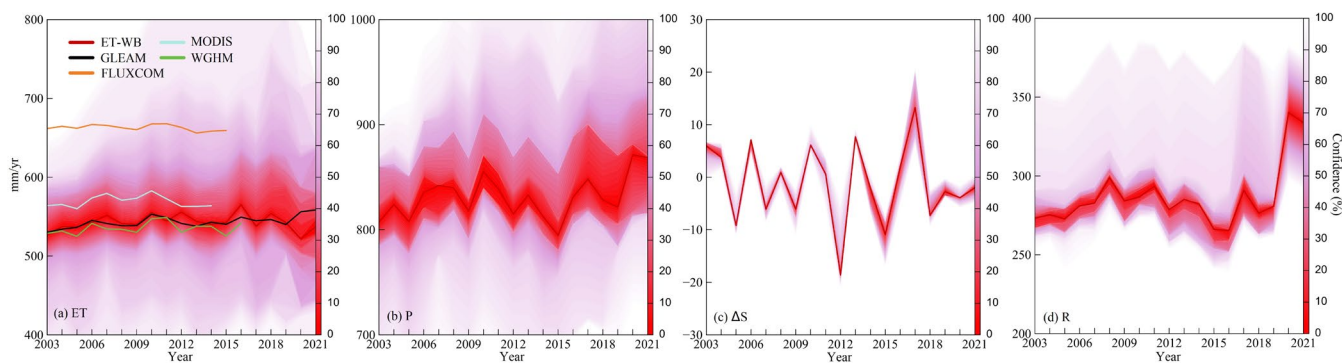
565 Inter-annual variability of ET and related water balance components are also examined over global land (Fig. 5). There are  
566 generally three episodes shown in the ET-WB dataset. These include a gradual increase from 2003 to 2010 and a subsequent  
567 decrease during 2010-2015, followed by a sharper reduction in the remaining years (Fig. 5a). A large inter-ensemble range,  
568 which aggravates during the recent time periods, due to the propagation of errors in monthly estimations of water balance ET  
569 is found. Other ET datasets, despite the different time spans, still present a similar variability to ET-WB with the  
570 overestimations in MODIS and FLUXCOM. As discussed above, the significant differences from FLUXCOM can be  
571 attributed to the specific data generation method. Furthermore, the annual variations of ET are typically explained by the  
572 changes in P, which experienced an increasing trend during 2003-2010, followed by an abrupt decrease between 2010 and  
573 2015 (Fig. 5b). However, the increase of P during 2015-2021 does not directly translate to the enhancement of ET based on  
574 ET-WB results, though the GLEAM shows a more ‘reasonable’ increase under the assumption of the limited influence of the  
575 human interventions on the global ET on an annual scale. This inconsistent phenomenon is because of the significant increase  
576 of R values since 2015 (particularly in 2020 and 2021), which are mainly driven by GloFAS reanalysis data as the 23 G-RUN  
577 ENSEMBLE subsets are not available from 2020 (Fig. 5d). Therefore, the overestimation of R in GloFAS data can explain the  
578 abrupt change in ET-WB over recent years, implying that caution should be taken when interpolating the ET-WB results after  
579 2019 due to the availability of the limited dataset. This is not only because of the controlling role of specific water components  
580 in ET-WB (e.g., a wide range of P similar to ET) but also the limited data availability due to delayed updates (e.g., G-RUN  
581 ENSEMBLE). Moreover,  $\Delta S$  does not play a crucial role on an annual scale because of the relatively small amplitude and the  
582 confident estimations of GRACE signals in such a large area (Fig. 5c).

583 Statistical metrics are re-assessed on an annual scale to evaluate the differing performance of ET-WB across temporal  
584 scales. A similar spatial pattern is revealed according to the RB results but slightly degrades over most basins, which is  
585 seemingly caused by error accumulation from water components and the relatively short time span for calculation (e.g., 19  
586 years) (Fig. 6). For the global land, the RB reaches -0.05%, -18.07%, -4.61%, and 1.73% for the GLEAM, FLUXCOM,  
587 MODIS, and WGHM, respectively. Alternate metrics such as CC and NSE also indicate deteriorating accuracy of ET-WB  
588 after converting from monthly to the annual time scale for the single basin, while RMSE is improved if we use the same unit  
589 (Figs. S5-S7). However, the scatter plots of annual ET in a total of 168 basins between ET-WB and auxiliary datasets show  
590 significant improvements to that on the monthly scale due to the offsets of negative ET values within a year and more benign  
591 fluctuations of annual ET than the monthly series. For example, the fitted slope of the regression between ET-WB and other  
592 datasets is 0.92 (GLEAM), 1.03 (FLUXCOM), 0.93 (MODIS), and 1.01 (WGHM), respectively, with higher CC and NSE  
593 compared with their monthly counterparts.

594



595



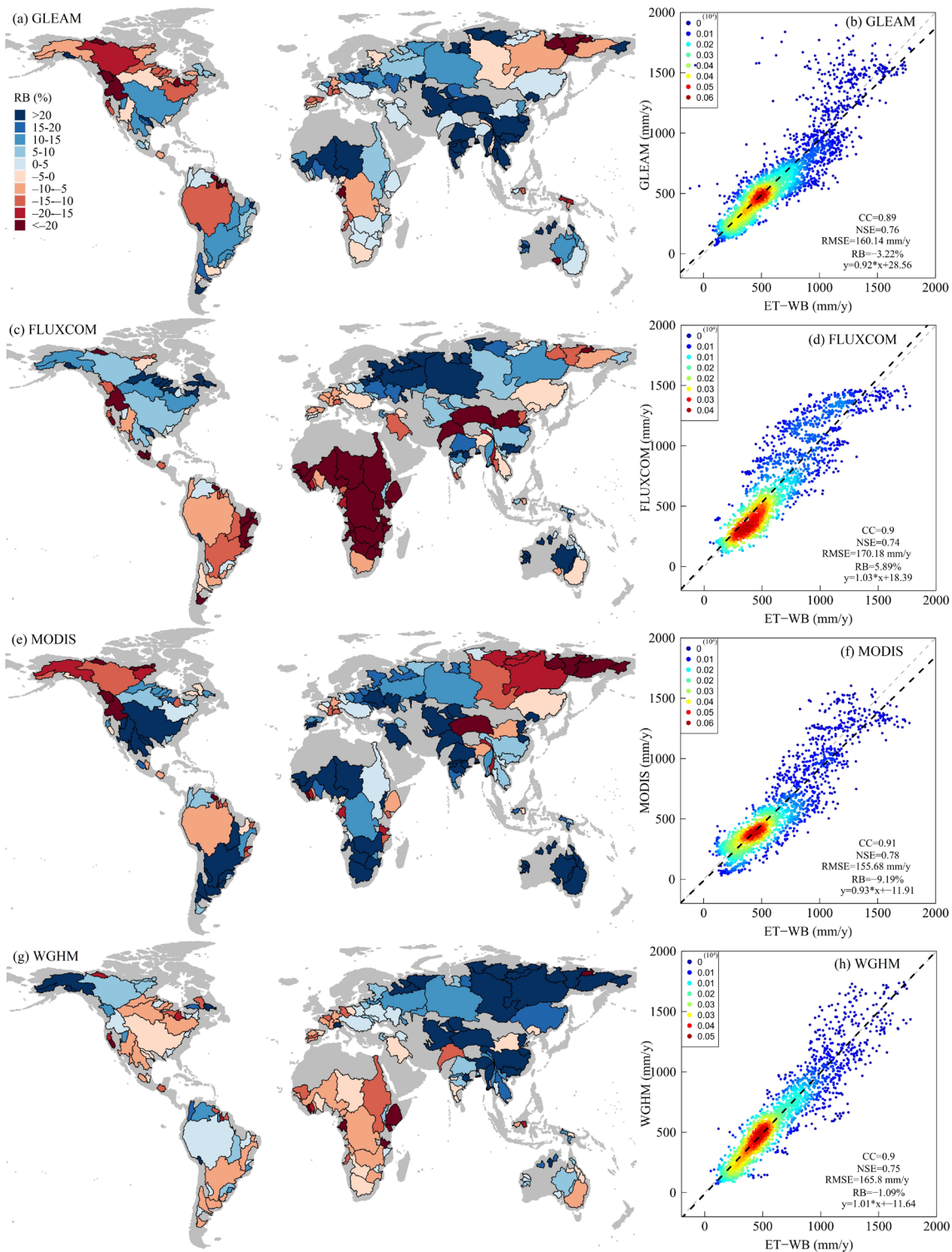
596

597

598

599

**Figure 5: Annual time series of ET-WB and multiple auxiliary ET products as well as other water components over global land during the period 2003-2021. The ET in 2002 is excluded from the calculation because of the missing values from January to April 2002. The shading shows the spread range among different datasets.**





601 **Figure 6: Comparisons between the ET-WB and multiple auxiliary ET products (a, b: GLEAM; c, d: FLUXCOM; e, f: MODIS; g,**  
602 **h: WGHM) on the annual scale during the period 2002–2021. The left column represents the global distribution of RB, and the right**  
603 **column represents the corresponding scatter plots. The color of the scatter points indicates the kernel density.**

604

#### 605 4.2 Spatiotemporal variation of ET-WB

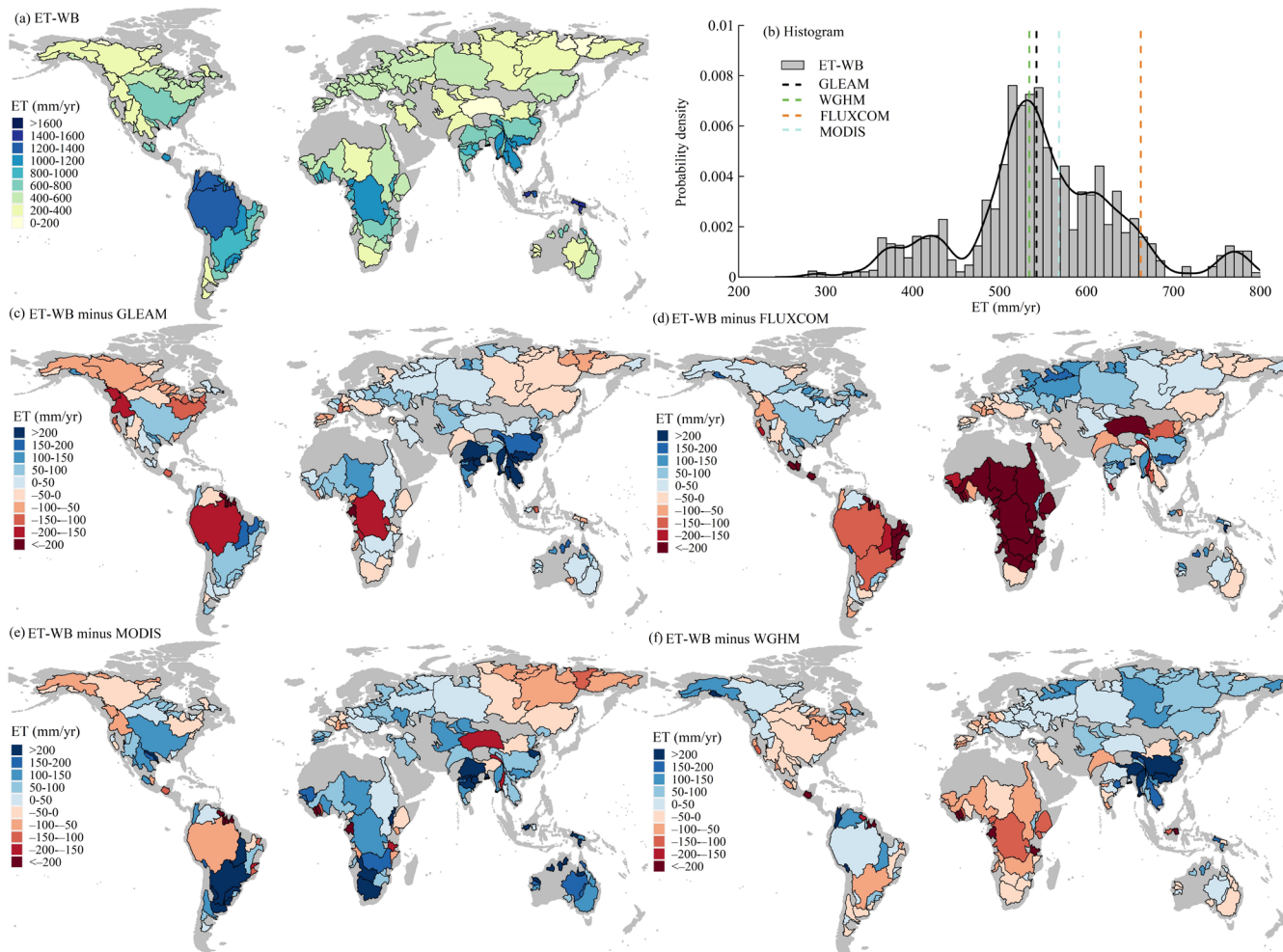
606 Spatiotemporal variability of ET from the ET-WB and other auxiliary ET products are assessed for comparison. The long-term  
607 mean of annual ET based on the ET-WB illustrates a clear spatial pattern, with relatively higher ET in humid zones of South  
608 America, Eastern North America, central South Africa, and South Asia, while the lower ET in arid regions of Western United  
609 States, North and South of Africa, Central Asia, and Australia (Fig. 7a). Specifically, the Kapuas River basin (ID: 131) in  
610 Indonesia has the highest ET-WB flux of 1565 mm/yr due to the hot and humid climate regionally (Hidayat et al., 2017). The  
611 endorheic Tarim River basin (ID: 14) in northwest China has the lowest annual ET of 127 mm/yr among 168 study basins  
612 because of the prevailing extremely dry climatic conditions. The homogeneous spatial patterns between ET-WB and GLEAM,  
613 FLUXCOM, and MODIS products can further validate the reliability of ET-WB (Fig. S8). In addition, WGHM reports a  
614 slightly different distribution from the other three datasets and ET-WB, which can result from modeling uncertainty due to  
615 simplified model parameterization and the un-calibrated ET simulations (Müller Schmied et al., 2021). Specifically, we  
616 observe the consistent overestimations of ET-WB than other datasets in East Europe, West Russia, South and East Asia, and  
617 West Australia, especially in the wet areas like the Yangtze (ID: 13) and Mekong (ID: 31) River basins. On the contrary,  
618 relative underestimations are observed in West Europe, East Russia, and Southeastern basins of Australia (Fig. 7). The  
619 divergent patterns between ET-WB and different datasets are seen in large-scale regions of South and North America, Africa,  
620 and Central Asia. Nevertheless, the regional differences are mostly within the range of  $\pm 100$  mm/yr, which is a relatively small  
621 range for basins with higher ET values, unlike the dry basins with relatively small ET (Figs. 7c-7f). The spatial distributions  
622 of differences between ET-WB and other datasets are similar to the RB results (Fig. 4), which manifests from the homologous  
623 calculation formula (Eq. 5). For the global land, the long-term mean annual ET estimates from ET-WB are concentrated within  
624 the range of 500-600 mm/yr among ensemble members, with the median estimates of 549 mm/yr (Fig. 7b). This number is  
625 comparable to the result from GLEAM (543 mm/yr), MODIS (569 mm/yr), and WGHM (534 mm/yr). The relatively higher  
626 value of global ET from FLUXCOM (663 mm/yr) is attributable to the exclusion of the unvegetated area in the global  
627 averaging, while it has shown good agreement with several global products (e.g., GLEAM) in the vegetated area (Jung et al.,  
628 2019).

629 The annual trends of ET from various datasets during 2003-2014 are assessed. The calculation period is selected to  
630 be consistent with the temporal span of different products, which can cause some biases in determining trends due to the  
631 relatively short computation period (i.e., 12 years). The ensemble median results of the ET-WB ensemble reveal a spatial  
632 distribution with the increasing ET detected in South America (around the Amazon River basin), Europe, East Russia, South  
633 and East Asia, South and North Africa, and Australia. Over these regions, the Burdekin River basin (ID: 94) in Australia has  
634 the most rapid growth rate of 31.4 mm/yr<sup>2</sup>, which is about 100 times the slowest increasing slope (0.3 mm/yr<sup>2</sup>) in the Alazeya



635 River basin (ID: 165) of Russia (Fig. 8a). Significant depletion of ET is observed in the central North America and Africa  
636 continents as well as West Russia with the lowest trend of  $-22.8 \text{ mm/yr}^2$  in the Moose River basin (ID: 107) of Canada. We  
637 also noticed similar spatial patterns based on other auxiliary ET datasets (Fig. S9), however, with the differences in the  
638 magnitudes of trends. Such differences are reasonable because the trend estimations contain uncertainty in a short 12-year long  
639 period, let alone the errors inherent to various products. Therefore, we see an interesting spatial distribution of the differences  
640 between ET-WB and other datasets (Figs. 8c-8f), where the regional differences in trends are similar to the actual trend  
641 summarized by the corresponding dataset (Fig. S9). In particular, ET-WB is prone to overestimate the trends for regions with  
642 increasing ET, and the overestimations are larger if the trends are larger (based on other ET datasets), and vice versa. In a  
643 nutshell, unlike TWS/P-based evaluation (Held and Soden 2006; Xiong et al., 2022b), the ‘dry gets drier and wet gets wetter’  
644 paradigm can be typically inferred from ET-WB on a basin scale, which generally exaggerates the prevailing  
645 increasing/decreasing ET tendencies in the basins (Yang et al., 2019). On a global scale, the median value of trend estimates  
646 from ET-WB ensemble members is  $1 \text{ mm/yr}^2$ , very close to the results from GLEAM ( $0.8 \text{ mm/yr}^2$ ) and WGHM ( $0.8 \text{ mm/yr}^2$ ).  
647 However, both FLUXCOM and MODIS report small negative values of  $-0.3$  and  $-0.1 \text{ mm/yr}^2$ , respectively, which still fall  
648 within the spread range of the ET-WB ensemble estimations (Fig. 8b).

649



650

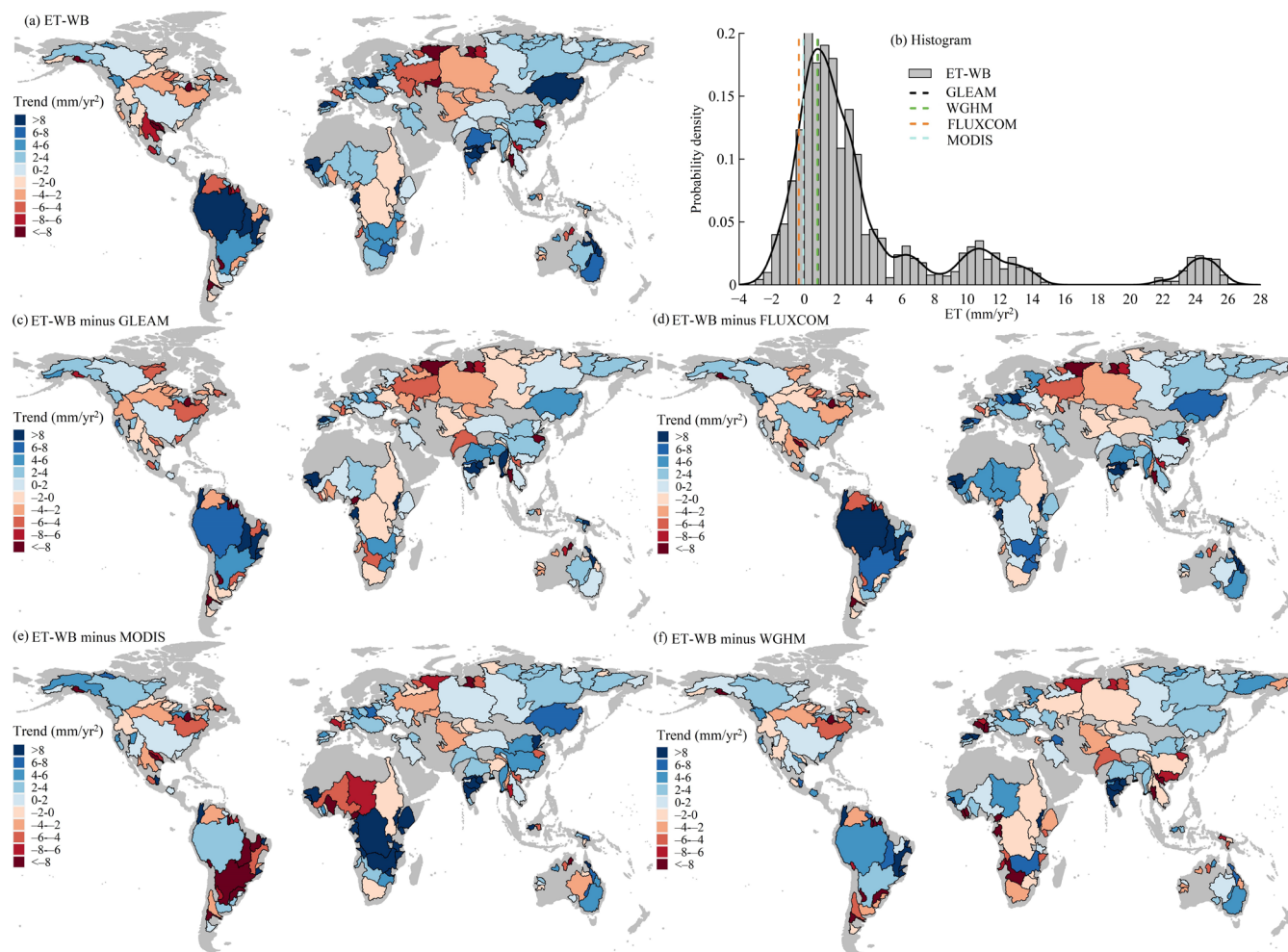
651

652

653

654

**Figure 7: Global distribution of (a) the long-term mean in annual ET-WB and (c-f) its difference with multiple auxiliary ET products during 2003–2021. The long-term mean is calculated as the sum of the long-term averages of ET in each month. Subplot (b) shows the histogram and the probability density distribution of the ET-WB ensemble results over global land.**



655

656 **Figure 8:** Same as Figure 7, but for the annual trends. The ET in 2002 and after 2014 are excluded from the calculation because of  
657 the missing values of GRACE data in 2002 and the missing values of MODIS product after 2014. The trend is calculated by using  
658 Sen's slope method. Subplot (b) shows the histogram and the probability density distribution of the ET-WB ensemble results over  
659 global land.

660

### 661 4.3 Uncertainty in ET-WB

662 Quantification and attribution of uncertainty in the ET-WB ensemble play important roles in the justification and potential  
663 usages of the proposed dataset. Based on the methods described in Section 2.3, we present the global distribution of the RMS  
664 values of uncertainty in ET-WB and related water components as well as the auxiliary ET products (Fig. 9). We observe a  
665 clear spatial pattern of the uncertainty, which generally increases along with the reduction in basin size. Several large-size  
666 basins, such as Ob (ID: 5), Yenisey (ID: 7), and Lena (ID: 9) River basins, possess a lower uncertainty ( $< 20$  mm/m) compared  
667 to those medium-size basins like Mekong (ID: 31) and Ganges (ID: 22) River basins where uncertainties in ET-WB are between

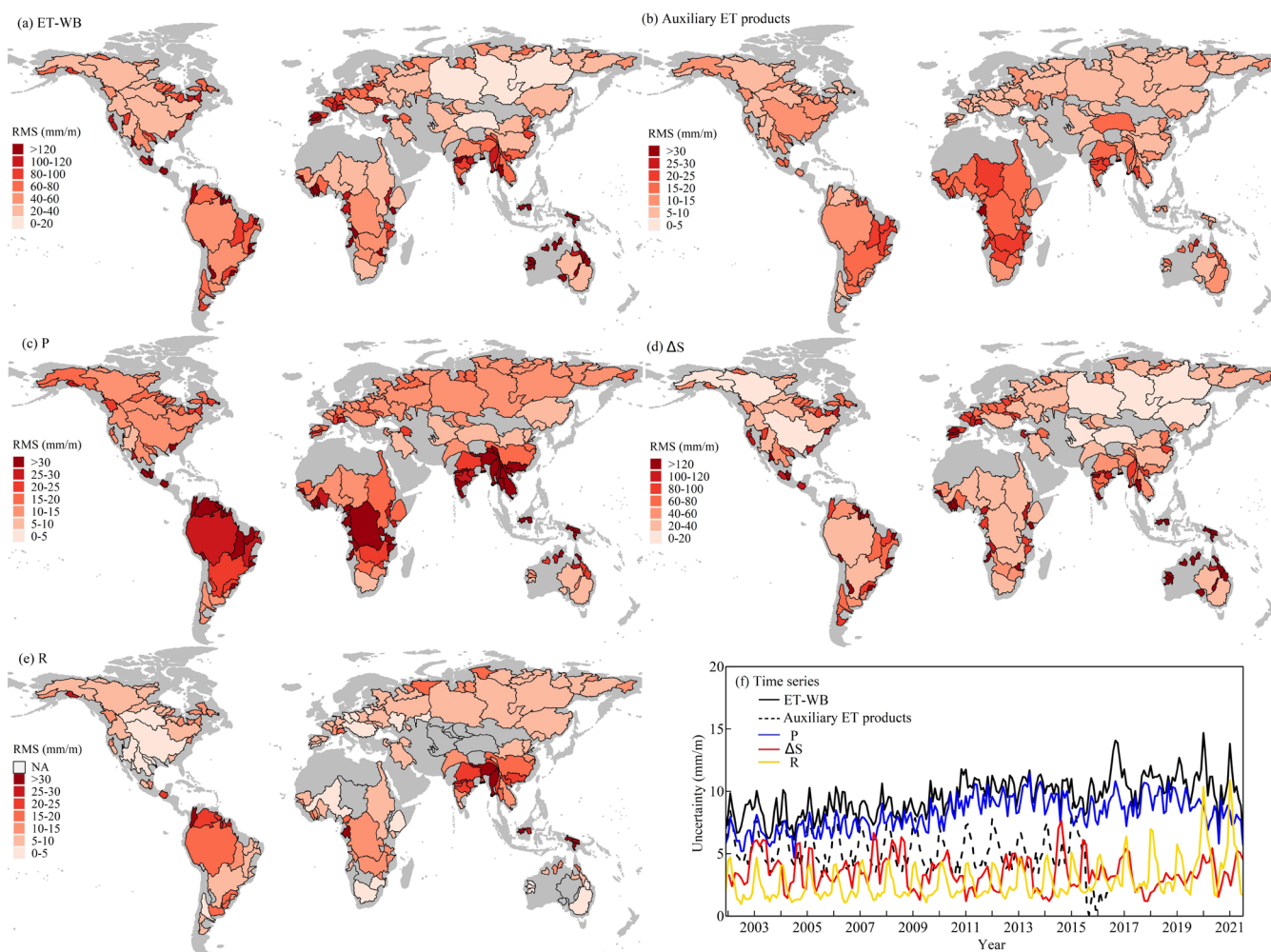


668 40 and 80 mm/m. However, the small-size basins suffer from substantial uncertainties in ET-WB, even exceeding 100 mm/m  
669 in some regions of mainland Australia and Europe (Fig. 9). The worst phenomenon happens in the Essequibo River basin (ID:  
670 156), with the RMS of the uncertainty of 267 mm/m primarily arising from the high uncertainties in GRACE data (Fig. 9a). A  
671 seemingly more optimistic situation is observed from the uncertainty of four auxiliary ET products, where the low-latitude  
672 humid zones apparently suffer from higher uncertainty than the high-latitude regions, though they are essentially smaller than  
673 30 mm/m with the maximum of 65 mm/m in the Ogooue River basin (ID: 68) of Gabon (Fig. 9c). It is not surprising because  
674 the uncertainty in ET-WB is propagated from three water components including P,  $\Delta S$ , and R, but that in the auxiliary ET  
675 products in our study is calculated as the standard deviation among four datasets. Despite this, the performance of ET-WB  
676 over large basins is still comparable to these ET datasets, whose uncertainties share similar spatial distribution with P to a  
677 certain degree. As an important input for GHM and some other ET products (e.g., “RS+METEO” setup of FLUXCOM), P can  
678 determine the actual performance of the auxiliary ET products. It can even determine the uncertainty in R datasets which  
679 subsequently contributes to the uncertainty of G-RUN ENSEMBLE; the main data for our water balance forcing (Figs. 9d and  
680 9f). However, the “reduction-with-increasing-size” pattern of uncertainty in ET-WB seems more relevant to the uncertainty in  
681  $\Delta S$  datasets, which is from six different GRACE solutions and a set of simulations from WGHM. It has been widely reported  
682 that the retrieval bias of GRACE missions is higher in smaller regions due to the coarse spatial resolution and the pronounced  
683 signal leakage effects (Scanlon et al., 2018) (Fig. 9e). This is contended to be the main reason for the similar distribution and  
684 amplitudes of uncertainty in  $\Delta S$  and ET-WB for smaller basins, while the uncertainty in ET-WB over larger basins is mainly  
685 controlled by other factors like P. However, over a global scale, the uncertainty of ET-WB that roughly fluctuates below 15  
686 mm/m (RMS: 9.7 mm/m) is controlled by that of P (RMS: 8.3 mm/m), the uncertainty in  $\Delta S$  is relatively small because of the  
687 very large area (Fig. 9b). The sharp increase in uncertainty of R from the year 2020 is caused by the unavailability of 23 G-  
688 RUN ENSEMBLE datasets. Similarly, the abrupt decrease of uncertainty in auxiliary ET products after 2015 is due to the  
689 limited time coverage of FLUXCOM and MODIS products, with an RMS of 5.3 mm/m over the whole period. This different  
690 behavior underscores the potential users to pay attention to the number of datasets used to produce ET-WB. In addition, ET-  
691 WB will be updated as the new/updated versions of these constituent datasets are released to constrain such uncertainties.

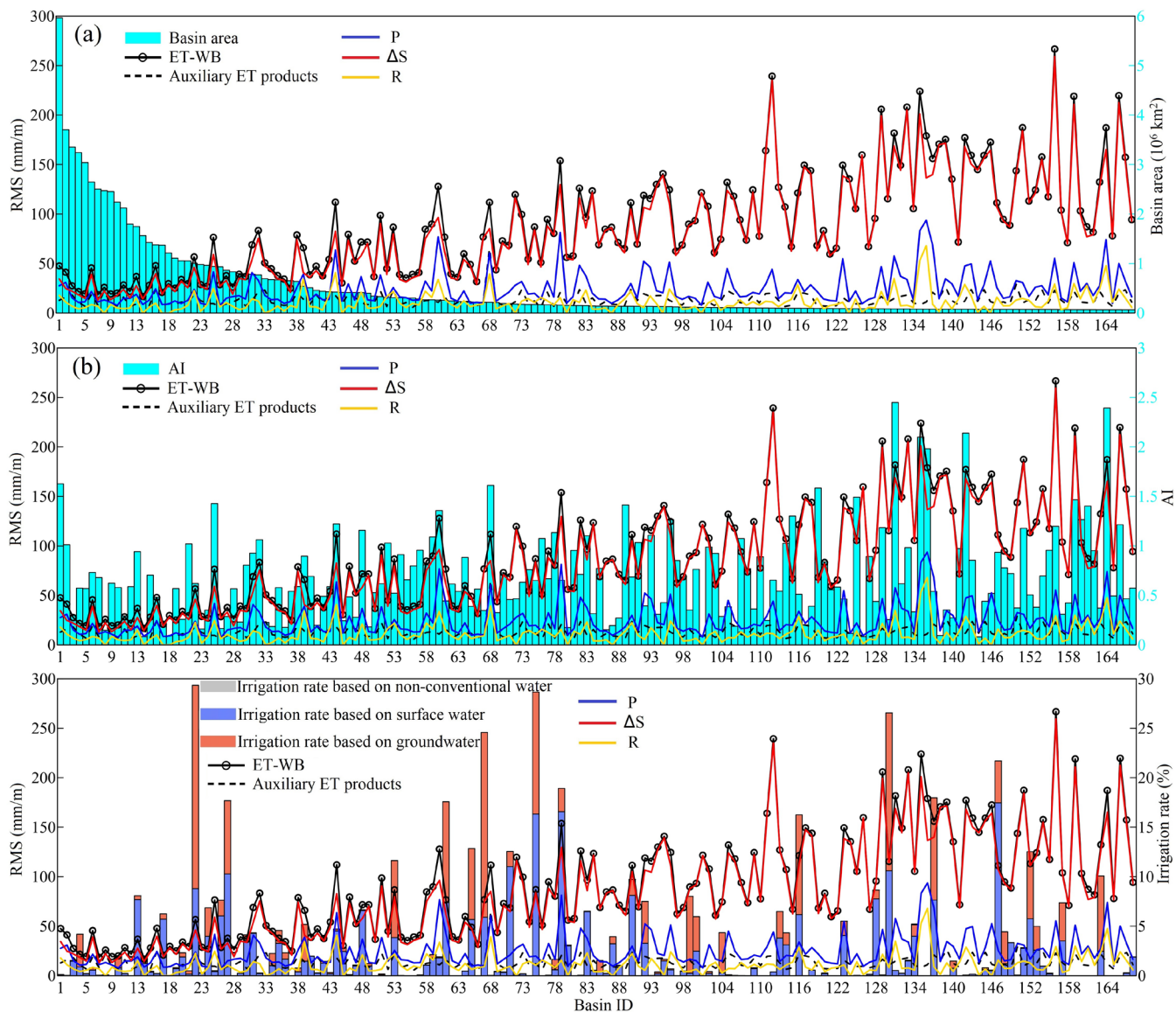
692 To further investigate the influential factors to the uncertainty in multiple variables, the relationship between the  
693 uncertainty and basin size, climate conditions (represented as the long-term mean AI), and human interventions (represented  
694 as the irrigation rate, which is defined as the equipped irrigation area versus the basin area) are detected (Fig. 10). As we  
695 described above, the obvious relationship between uncertainty in  $\Delta S$  and basin size governs the increasing uncertainty of ET-  
696 WB along with the enhancement of basin area, while the uncertainty in auxiliary ET products generally keep at a lower level  
697 of uncertainty similar to P and R (Fig. 10a). Although other variables like P and R do not show any pattern associated to the  
698 basin area, they present favorable dependence upon the aridity of the basin, where they are inclined to have higher uncertainty  
699 in more humid regions with higher AI (Fig. 10b). No clear pattern between ET uncertainty and irrigation area can be apparently  
700 deduced, whereas it is worth mentioning that the significant irrigation equipped for groundwater resources can lead to  
701 significant short-term and long-term variations of, for example,  $\Delta S$  and R, which is the case in some basins in North China



702 (e.g., Haihe River basin, ID: 67) and North India (e.g., Indus River basin, ID: 27) (Fig. 10c). The human-induced inordinate  
 703 fluctuations of water balance (e.g., through reservoir management, groundwater extraction) can influence the quality of ET-  
 704 WB by impacting the accuracy of the specific forcing variable (e.g., R). Finally, the uncertainty in ET-WB can be further  
 705 intensified for the small wet basins with significant human disturbance, so caution should be particularly taken when drawing  
 706 scientific conclusions using ET-WB in those regions.



707  
 708 **Figure 9: RMS of uncertainty in the ET-WB and different water components over global basins. Subplot (b) shows the time series**  
 709 **of uncertainty in different variables over global land. The NA values in sub-plot (f) R are because the runoff is manually set as zero**  
 710 **in these regions. Please refer to the Data section for details.**



711

712 **Figure 10: Relationship between RMS of uncertainty in the ET-WB, auxiliary ET products, different water balance components,**  
 713 **and (a) size, (b) aridity index, and (c) irrigation rate of the basins.**

714 **5 Discussions**

715 **5.1 Comparisons with previous regional studies**

716 Although a global compilation of water balance estimations of ET is still lacking, previous regional studies have demonstrated  
 717 the applicability of the water balance ET at different basins of the world. Comparisons with such regional studies are beneficial  
 718 to the benchmark of ET-WB. Rodell et al. (2004) initially proposed the plan to retrieve ET on basin scales based on the water



719 balance model and early GRACE data and applied it in the Mississippi River basin (ID: 4) from July 2002–November 2003.  
720 By comparing with model predictions of ET, the RMS differences between water balance ET and GLDAS, GRDS, and  
721 ECMWF-based ET were found to be 0.83, 0.67, and 0.65 mm/day (equivalent to 24.9, 20.1, and 19.5 mm/m), respectively  
722 (Rodell et al., 2004), which are comparable to our RMSE results on the monthly scale, i.e., 19.46 (GLEAM), 18.41  
723 (FLUXCOM), 24.29 (MODIS), and 23.04 (WGHM) mm/m. Given the significance of the water balance method in ungauged  
724 regions, several studies have tested its performance in the data-sparse Tibetan Plateau (Xue et al., 2013; Li et al., 2014; Li et  
725 al., 2019). For example, Xue et al. (2013) compared four ET products, including GLDSA, JRA, MODIS, and Zhang\_ET  
726 (Zhang et al., 2010), against the water balance ET in the upper Yellow (ID: 24) and Yangtze (ID: 13) River basins, revealing  
727 the overestimations of GLEAM and MODIS relative to the water balance ET. These comparisons are similar to the RB  
728 examinations in our study based on ET-WB. As the largest river basin of India that accounts for 26% of the country’s landmass,  
729 the Ganges River basin (ID: 22) shows a mean monthly average ET of 63.2 mm/m (Syed et al., 2014), which is comparable to  
730 60.9 mm/m calculated in our study despite the different study periods. A case study in the Volta River basin (ID: 46) of Africa  
731 reported the annual fluctuations of water balance ET ranging from 700 to 800 mm/yr during the period 2004–2011 (Andam-  
732 Akorful et al., 2015), relatively lower than the long-term mean ET-WB of 830 mm/yr. The relative accuracy of water balance  
733 ET in the exorheic river basins of China has also been previously evaluated. For example, Zhong et al. (2020) employed the  
734 water balance equation to estimate regional ET and compared them with the GLEAM and GLDAS products, concluding the  
735 uncertainty of monthly ET of 14.7 mm/m in the Yellow River basin (ID: 24) and 35.9 mm/m in the Pearl River basin (ID: 48),  
736 nearly half of the estimates in our study, i.e., 27.0 and 71.7 mm/m in these basins, respectively, primarily due to different  
737 datasets and methods used. We note these regional studies generally used observed and typically single-source water  
738 components data like P and R, which can be the reason for the differences with our results based on multi-source data-based  
739 calculations. Moreover, the difference in study region boundaries, data processing algorithms, calculation scheme of the  
740 terrestrial water storage change, and time period may reflect the disparities in the estimates (Rodell et al., 2004).

741 A few global analyses can also provide an important reference for the ET-WB developed in our study. Specifically,  
742 Zeng et al. (2012) collected in-situ runoff, precipitation, and GRACE data to estimate ET over 59 major river basins during  
743 2003–2009, highlighting the fact that  $\Delta S$  cannot be neglected in the water balance computations. This finding implies the  
744 importance of including GRACE TWSA ( $\Delta S$ ) in the water balance closure at basin scales. Ramillien et al. (2006) applied the  
745 GRACE samplings, GPCC precipitation, and modeled runoff to estimate ET time series over 16 drainage basins of the world,  
746 in which the extreme errors (1.8 mm/day, 50% relative error) as expected by the accuracy of model runoff in the Amazon (ID:  
747 1) River basin, is emphasized to influence the regional ET estimations. This well corresponds to the high uncertainty estimates  
748 of P, R, and therefore ET-WB in both long-term mean and annual trend levels of our study. Similar to the examinations of  
749 long-term mean and annual trends in our study, a previous global evaluation of water balance ET estimates against nine ET  
750 products over 35 basins points out that water balance ET can reasonably estimate the annual means (especially in dry zones  
751 with relatively lower uncertainty) but substantially underestimated the inter-annual variability in terms of annual trends and  
752 mean annual standard deviation (Liu et al., 2016). Furthermore, the comprehensive uncertainty analysis for ET products from



753 four LSMs in NLDAS, two remote-sensing-based products including MODIS and AVHRR, and water balance estimations  
754 show the highest uncertainty in the latter (20-30 mm/m) over the different climatic regions (from humid to arid) in South  
755 Central United States (Long et al., 2014). The finding confirms the pattern of obviously higher uncertainty in ET-WB than  
756 auxiliary ET products in several arid basins in Western United States in our study. A recently published global ET product  
757 based on the three-temperature model used the water balance ET in 34 catchments worldwide as a benchmarking product,  
758 revealing the RB mostly ranging from -25 to 25% on the annual scale, with the underestimation of water balance ET in high  
759 latitudes (Yu et al., 2022). The comparisons are quite relevant to the results of ET-WB, which also underestimates ET in East  
760 Russia and Northern North America by comparing with, for example, GLEAM and MODIS products. Overall, the results of  
761 our proposed ET-WB datasets are consistent with previous regional and global studies, more importantly, cover the most recent  
762 time periods, and provide observational constraints to the global and regional ET leveraging huge datasets of water balance  
763 components.

## 764 **5.2 Implications, limitations, and future outlook**

765 The production of ET-WB ensemble datasets can benefit the future hydrological community in various ways. First of all, the  
766 ET-WB can provide valuable information for the regional ET variations, greatly enriching the existing ET datasets consisting  
767 of the remote-sensing-based (e.g., MODIS), LSM-predicted (e.g., GLDAS), GHM-predicted (e.g., WGHM), observation-  
768 driven (e.g., FLUXCOM), in-situ-based (e.g., eddy tower observations) and other diagnostic datasets (e.g., GLEAM) as well  
769 as the synthetic datasets. Given the non-ignorable differences among the existing ET datasets and an independent mass  
770 conservation-based ET-WB, it can not only help to benchmark other datasets/models of ET but will also contribute to the  
771 validation and calibration of hydrological models across scales. This is particularly useful for poorly gauged regions like the  
772 Qinghai-Tibetan Plateau, African river basins, and high-latitudes cold regions, where the installation and maintenance of the  
773 field observation network are quite challenging (Li et al., 2019). In addition, the ET-WB product will provide additional  
774 information for evaluating water balance closure on the basin and global scales (Lehmann et al., 2022). The ET-WB dataset  
775 that generates ET based on the terrestrial water balance is also dedicated to evaluating other water balance components like R  
776 by combining them with the available hydrological records (e.g., P) regionally or globally (Syed et al., 2010; Chandanpurkar  
777 et al., 2017). Finally, the ET-WB product is conducive to detecting human footprints in the regional water cycle. For example,  
778 Pan et al. (2017) combined the water balance estimations of actual ET and the modeling results without consideration of human  
779 activities to estimate human-induced ET in a highly developed region of China (Haihe River basin), implying a 12% increase  
780 of ET due to human activities such as irrigation. Strong influences of anthropogenic changes to the region ET were also  
781 reported in the Colorado River basin of western United States (Castle et al., 2016). Overall, the developed ET-WB has the  
782 potential to support multi-discipline applications in hydrology and climate fields.

783 However, the ET-WB also suffers from a few limitations mainly related to the uncertainty, selection, and assumptions  
784 of datasets involved in water balance computations. As shown in comparison with other ET datasets and the uncertainty  
785 analysis, propagated uncertainty from different variables like  $\Delta S$  and P can greatly influence the quality of ET estimations. For



786 example, the relatively higher uncertainty of GRACE signals in smaller basins increases after the derivation of  $\Delta S$  subsequently  
787 alters the estimations of ET. Biases in P over humid zones can also play an important role in the performance of regional ET.  
788 In terms of R, since only one of the 29 subsets is from the in-situ discharge and mostly are provided by the observation-driven  
789 machine learning G-RUN ENSEMBLE dataset with varying forcings, the ET estimations for the basins without in-situ  
790 observations might be biased. Further, the G-RUN ENSEMBLE, as a gridded runoff rate product purely forced by  
791 meteorological data, does not physically account for human activities (e.g., dam management) into consideration. Such  
792 simplicities might overestimate or underestimate the actual runoff for the basins with significant human intervention, with the  
793 underlying assumption that the water loss in river channels can be neglected to convert runoff into river streamflow on a  
794 monthly scale. Overall, the inherent uncertainties in multiple water cycle components (P,  $\Delta S$ , and R) can propagate to the ET-  
795 WB product.

796 To overcome the multisource uncertainties, several suggestions for future use and improvements are provided as  
797 follows: (1) appropriate consideration of human disturbances such as water diversion in water balance estimates of ET should  
798 be highlighted in specific regions (e.g., the South-to-North Water Diversion Project across South and North China); (2)  
799 considering the significant role of the forcing data in determining the accuracy of ET-WB, careful justification of different  
800 inputs (e.g., P) that have better performance for the regions of interest should be performed in combination of regional in-situ  
801 observations; (3) future efforts should incorporate in-situ ET observations from regional eddy covariance towers with  
802 calibration, assimilation, and correction procedures to improve further the accuracy of ET-WB (Billah et al., 2015); (4)  
803 integrated ET products that consider a hybrid approach to integrate strengths of different categories of data, including ET-WB  
804 and satellite products, are worthy of being proposed to further constrain the uncertainties in regional ET (Long et al., 2014).

## 805 **6 Data availability**

806 All the datasets used in our study are publically available online and have been introduced in the Data section. The ET-WB  
807 dataset is also publicly available in the Version 7.3 MAT-files (Xiong et al., 2023) and can be freely downloaded on the Zenodo  
808 platform (doi:10.5281/zenodo.7314920).

## 809 **7 Conclusions**

810 In the current study, a global monthly ET product (named ET-WB) over 168 river basins that account for ~60% of the Earth's  
811 land area except for Greenland and Antarctic ice sheets and global land during May 2002-December 2021, is developed based  
812 on the water balance equation employing 23 precipitation, 29 runoff, and 7  $\Delta S$  datasets from satellite products, in-situ  
813 measurements, reanalysis, and hydrological simulations. The performance of ET-WB has been evaluated against four auxiliary  
814 global ET datasets comprising the GLEAM, FLUXCOM, MODIS, and WGHM at various time scales based on different  
815 statistical metrics (i.e., CC, NSE, RMSE, and RB). The long-term mean and annual trend of ET-WB and above ET products



816 are also assessed. Uncertainty of ET-WB is quantified by propagating the errors in different water components, and its  
817 relationships with basin size, climate aridity, and human irrigation are also investigated.

818 The seasonal cycles of the ET-WB ensemble, mainly dominated by precipitation, generally agree with multiple ET  
819 global products despite the overestimations/underestimations in specific months compared with the median ET-WB results.  
820 Inter-annual variability of global land ET-WB presents a gradual increase from 2003 to 2010 and a subsequent decrease during  
821 2010-2015, followed by a sharper reduction in the remaining years due to the varying P, similar to other ET products. However,  
822 the increase of P during 2015-2021 does not translate to the enhancement of ET because of the overestimated GloFAS  
823 reanalysis and the limited data availability (e.g., G-RUN ENSEMBLE) in the period. Multiple statistical metrics show  
824 reasonably good accuracy of ET-WB, with most river basins having RB between -20% and 20% on a monthly scale. The  
825 performance improves on an annual scale but with strong spatial heterogeneity among different basins.

826 The long-term mean annual ET estimates from ET-WB are concentrated within the range of 500-600 mm/yr among  
827 ensemble members with the median estimates of 549 mm/yr for global land, comparable to the result from GLEAM (543  
828 mm/yr), MODIS (569 mm/yr), and WGHM (534 mm/yr). The relatively higher value from FLUXCOM (663 mm/yr) can be  
829 attributed to the non-consideration of the unvegetated area. Regarding annual trends, the ‘dry gets drier and wet gets wetter’  
830 paradigm can be inferred from ET-WB, which generally exaggerates the prevailing increasing/decreasing ET in basins. On a  
831 global scale, the median value of trend estimates from ET-WB ensemble members is 1 mm/yr<sup>2</sup>, close to the results from  
832 GLEAM (0.8 mm/yr<sup>2</sup>) and WGHM (0.8 mm/yr<sup>2</sup>). However, both FLUXCOM and MODIS report small negative values of -  
833 0.3 and -0.1 mm/yr<sup>2</sup>, respectively, still within the ET-WB ensemble spread range.

834 The uncertainty of ET-WB that roughly fluctuates below 15 mm/m (RMS: 9.7 mm/m) is primarily controlled by that  
835 of P (RMS: 8.3 mm/m), which is relatively higher than the auxiliary ET products (RMS: 5.3 mm/m) over global land. The  
836 inversely proportional relationship between uncertainty in  $\Delta S$  and basin size governs the increasing uncertainty of ET-WB  
837 along with the enhancement of basin area. Other variables like P and R present relative dependence upon the basin’s aridity,  
838 where they are inclined to have higher uncertainty in more humid regions with higher AI. Moreover, the significant irrigation  
839 equipped for groundwater resources can lead to significant short-term, and long-term variations of, for example,  $\Delta S$  and R,  
840 which is the case of some basins in North China (e.g., Haihe River basin (ID: 67)) and North India (e.g., Indus River basin (ID:  
841 27)). The uncertainty in ET-WB can be further intensified for the small wet basins with significant human disturbance, so  
842 caution should be taken when drawing the scientific conclusions using ET-WB over those regions.

#### 843 **Author contributions**

844 Jinghua Xiong contributed to the data processing. Jinghua Xiong and Abhishek conducted the research and wrote the original  
845 draft and revised it. Gionata Ghiggi and Yun Pan contributed to the conceptual design and review of the manuscript. Shenglian  
846 Guo contributed to the funding acquisition and project administration. All co-authors reviewed and revised the manuscript.



847 **Competing interests**

848 The authors declare that they have no conflict of interest.

849 **Acknowledgments**

850 We thank Dr. Shuang Yi from the University of Chinese Academy of Sciences for providing the reconstructed GRACE data.

851 **Financial support**

852 Our study was financially supported by the National Natural Science Foundation of China (U20A20317) and the National Key  
853 Research and Development Program of China (2022YFC3202801).

854 **References**

- 855 Abhishek, Kinouchi, T. and Sayama, T.: A comprehensive assessment of water storage dynamics and hydroclimatic extremes  
856 in the Chao Phraya River Basin during 2002–2020, *J. Hydrol.*, 603, doi:10.1016/j.jhydrol.2021.126868, 2021.
- 857 Alfieri, L., Lorini, V., Hirpa, F. A., Harrigan, S., Zsoter, E., Prudhomme, C., and Salamon, P.: A global streamflow reanalysis  
858 for 1980–2018, *J. Hydrol. X*, 6, 100049, doi:10.1016/j.hydroa.2019.100049, 2020.
- 859 Andam-Akorful, S. A., Ferreira, V. G., Awange, J. L., Forootan, E., and He, X. F.: Multi-model and multi-sensor estimations  
860 of evapotranspiration over the Volta Basin, West Africa, *Int. J. Climatol.*, 35, 3132–3145, doi:10.1002/joc.4198, 2015.
- 861 Ashouri, H., Hsu, K. L., Sorooshian, S., Braithwaite, D. K., Knapp, K. R., Cecil, L. D., Nelson, B. R., and Prat, O. P.:  
862 PERSIANN-CDR: Daily precipitation climate data record from multisatellite observations for hydrological and climate studies,  
863 *B. Am. Meteorol. Soc.*, 96, 69–83, doi:10.1175/BAMS-D-13-00068.1, 2015.
- 864 Baker, J. C. A., Garcia-Carreras, L., Gloor, M., Marsham, J. H., Buermann, W., da Rocha, H. R., Nobre, A. D., de Araujo, A.  
865 C., and Spracklen, D. V.: Evapotranspiration in the Amazon: spatial patterns, seasonality, and recent trends in observations,  
866 reanalysis, and climate models, *Hydrol. Earth Syst. Sci.*, 25, 2279–2300, doi:10.5194/hess-25-2279-2021, 2021.
- 867 Beck, H., Wood, E., Pan, M., Fisher, C., van Dijk, D. M. A., and Adler, T. M. R.: MSWEP V2 global 3-hourly 0.1 precipitation:  
868 methodology and quantitative assessment, *B. Am. Meteorol. Soc.*, 0, 473–500, 2019.
- 869 Bhattarai, N., Mallick, K., Stuart, J., Vishwakarma, B. D., Niraula, R., Sen, S., and Jain, M.: An automated multi-model  
870 evapotranspiration mapping framework using remotely sensed and reanalysis data, *Remote Sens. Environ.*, 229, 69–92,  
871 <https://doi.org/10.1016/j.rse.2019.04.026>, 2019.
- 872 Billah, M. M., Goodall, J. L., Narayan, U., Reager, J., Lakshmi, V., and Famiglietti, J. S.: A methodology for evaluating  
873 evapotranspiration estimates at the watershed-scale using GRACE, *J. Hydrol.*, 523, 574–586, 2015.



- 874 Bodo, B. A.: Annotations for monthly discharge data for world rivers (excluding former Soviet Union), NCAR, 85, pp.,  
875 <http://dss.ucar.edu/datasets/ds552.1/docs/>, 2001.
- 876 Castle, S. L., Reager, J. T., Thomas, B. F., Purdy, A. J., Lo, M., Famiglietti, J. S. and Tang, Q.: Remote detection of water  
877 management impacts on evapotranspiration in the Colorado River basin, *Geophys. Res. Lett.*, 43, 5089–5097,  
878 doi:10.1002/2016GL068675, 2016.
- 879 Chandanpurkar, H. A., Reager, J. T., Famiglietti, J. S., Syed, T. H. Satellite- and reanalysis-based mass balance estimates of  
880 global continental discharge (1993–2015), *J. Clim.*, 30 (21), pp. 8481–8495, doi:10.1175/JCLI-D-16-0708.1, 2017.
- 881 Chen, M., and Xie, P.: CPC Unified gauge-based analysis of global daily precipitation, in: Western Pacific Geophysics  
882 Meeting, Cairns, Australia, 29 July - 1 August, 2008.
- 883 Chen, J., Tapley, B., Seo, K.-W., Wilson, C., and Ries, J.: Improved quantification of global mean ocean mass change using  
884 GRACE satellite gravimetry measurements, *Geophys. Res. Lett.*, 46, 13984–13991, doi:10.1029/2019GL085519, 2019.
- 885 Cleveland, R. B., Cleveland, W. S., McRae, J. E., and Terpenning, I.: STL: A seasonal-trend decomposition procedure based  
886 on loess, *J. Official Statistics*, 6, 3–73, 1990.
- 887 Dai, A., and Trenberth, K. E.: Estimates of freshwater discharge from continents: Latitudinal and seasonal variations, *J.*  
888 *Hydrometeor.*, 3, 660–687, 2002.
- 889 Do, H. X., Gudmundsson, L., Leonard, M., and Westra, S.: The global streamflow indices and metadata archive (GSIM) – Part  
890 1: The production of a daily streamflow archive and metadata, *Earth Syst. Sci. Data*, 10, 765–785, doi:10.5194/essd-10-765-  
891 2018, 2018.
- 892 Dong, B., and Dai, A.: The uncertainties and causes of the recent changes in global evapotranspiration from 1982 to 2010.  
893 *Climate Dynamics*, 49(1-2), 279–296, 2017.
- 894 Döll, P., Müller Schmied, H., Schuh, C., Portmann, F. T., and Eicker, A.: Global-scale assessment of groundwater depletion  
895 and related groundwater abstractions: Combining hydrological modeling with information from well observations and GRACE  
896 satellites, *Water Resour. Res.*, 50, 5698–5720, doi:10.1002/2014WR015595, 2014.
- 897 Douville, H., Ribes, A., Decharme, B., Alkama, R., and Sheffield, J.: Anthropogenic influence on multidecadal changes in  
898 reconstructed global evapotranspiration. *Nat. Clim. Chang.* 3, 39–62, 2013.
- 899 Fisher, J., Melton, F., Middleton, E., Hain, C., Anderson, M., Allen, R., McCabe, M. F., Hook, S., Baldocchi, D., Townsend,  
900 P. A., Kilic, A., Tu, K., Miralles, D. D., Perret, J., Lagouarde, J., Waliser, D., Purdy, A. J., French, A., Schimel, D., Famiglietti,  
901 J. S., Stephens, G., and Wood, E. F.: The future of evapotranspiration: global requirements for ecosystem functioning, carbon  
902 and climate feedbacks, agricultural management, and water resources, *Water Resour. Res.*, 53, 2618–2626, 2017.
- 903 Funk, C., Peterson, P., Landsfeld, M., Pedreros, D., Verdin, J., Shukla, S., Husak, G., Rowland, J., Harrison, L., and Hoell, A.:  
904 The climate hazards infrared precipitation with stations – a new environmental record for monitoring extremes, *Scientific Data*,  
905 2, 150066, doi:10.1038/sdata.2015.66, 2015.
- 906 Ghiggi, G., Humphrey, V., Seneviratne, S. I., and Gudmundsson, L.: GRUN: an observation-based global gridded runoff  
907 dataset from 1902 to 2014, *Earth Syst. Sci. Data*, 11, 1655–1674, doi:10.5194/essd-11-1655-2019, 2019.



- 908 Ghiggi, G., Humphrey, V., Seneviratne, S., and Gudmundsson, L.: G-RUN ENSEMBLE: A Multi-Forcing Observation-Based  
909 Global Runoff Reanalysis, *Water Resour. Res.*, 57, e2020WR028787, doi:10.1029/2020WR028787, 2021.
- 910 Gibson, P. B., Waliser, D. E., Lee, H., Tian, B., and Massoud, E.: Climate model evaluation in the presence of observational  
911 uncertainty: Precipitation indices over the contiguous United States, *J. hydrometeor.*, 20, 1339–1357, 2019.
- 912 Good, S. P., Noone, D., and Bowen, G.: Hydrologic connectivity constrains partitioning of global terrestrial water fluxes,  
913 *Science*, 349, 175–177, <https://doi.org/10.1126/science.aaa5931>, 2015.
- 914 Harrigan, S., Zsoter, E., Alfieri, L., Prudhomme, C., Salamon, P., Wetterhall, F., Barnard, C., Cloke, H., and Pappenberger,  
915 F.: GloFAS-ERA5 operational global river discharge reanalysis 1979–present, *Earth Syst. Sci. Data*, 12, 2043–2060,  
916 doi:10.5194/essd-12-2043-2020, 2020.
- 917 Harris, I., Osborn, T. J., Jones, P., and Lister, D.: Version 4 of the CRU TS monthly high-resolution gridded multivariate  
918 climate dataset, *Sci. Data*, 7, 109, doi:10.1038/s41597-020-0453-3, 2020.
- 919 He, X., Pan, M., Wei, Z., Wood, E. F., and Sheffield, J.: A global drought and flood catalogue from 1950 to 2016, *B. Am.*  
920 *Meteorol. Soc.*, 101, E508–E535, doi:10.1175/bams-d-18-0269.1, 2020.
- 921 Held, I. M. and Soden, B. J.: Robust responses of the hydrological cycle to global warming, *J. Climate*, 19, 5686–5699, 2006.
- 922 Hersbach, H., Bell, B., Berrisford, P., Hirahara, S., Horányi, A., Muñoz-Sabater, J., Nicolas, J., Peubey, C., Radu, R., and  
923 Schepers, D.: The ERA5 global reanalysis, *Q. J. Roy. Meteorol. Soc.*, 146, 1999–2049, 2020
- 924 Hidayat, H., Teuling, A. J., Vermeulen, B., Taufik, M., Kastner, K., Geertsema, T. J., Bol, D. C. C., Hoekman, D. H., Haryani,  
925 G. S., Van Lanen, H. A. J., Delinom, R. M., Dijkema, R., Anshari, G. Z., Ningsih, N. S., Uijlenhoet, R., and Hoitink, A. J. F.:  
926 Hydrology of inland tropical lowlands: the Kapuas and Mahakam wetlands, *Hydrol. Earth Syst. Sci.*, 21, 2579–2594,  
927 <https://doi.org/10.5194/hess-21-2579-2017>, 2017.
- 928 Hirpa, F. A., Salamon, P., Beck, H. E., Lorini, V., Alfieri, L., Zsoter, E., and Dadson, S. J.: Calibration of the global flood  
929 awareness system (GloFAS) using daily streamflow data, *J. Hydrol.*, 566, 595–606, doi:10.1016/j.jhydrol.2018.09.052, 2018.
- 930 Hobeichi, S., Abramowitz, G., Evans, J., and Beck, H. E.: Linear optimal runoff aggregate (LORA): a global gridded synthesis  
931 runoff product, *Hydrol. Earth Syst. Sci.*, 23, 851–870, <https://doi.org/10.5194/hess-23-851-2019>, 2019.
- 932 Huffman, G. J., Bolvin, D. T., Nelkin, E. J., Wolff, D. B., Adler, R. F., Gu, G., Hong, Y., Bowman, K. P., and Stocker, E. F.:  
933 The TRMM multisatellite precipitation analysis (TMPA): quasi-global, multiyear, combined-sensor precipitation estimates at  
934 fine scales, *J. hydrometeor.*, 8, 38–55, doi:10.1175/JHM560.1, 2007.
- 935 Huffman, G. J., Stocker, E. F., Bolvin, D. T., Nelkin, E. J. and Tan, J.: GPM IMERG Final Precipitation L3 Half Hourly 0.1-  
936 degree x 0.1-degree V06, Greenbelt, MD, Goddard Earth Sciences Data and Information Services Center (GES DISC),  
937 Accessed: [2022/8/12]. doi:10.5067/GPM/IMERG/3B-HH/06, 2019.
- 938 Huffman, G. J., Behrangi, A., Bolvin, D. T. and Nelkin E. J.: GPCP Version 3.2 satellite-gauge (SG) combined precipitation  
939 data set, edited by Huffman, G. J., Behrangi, A., Bolvin, D. T., and Nelkin, E. J. Greenbelt, Maryland, USA, Goddard Earth  
940 Sciences Data and Information Services Center (GES DISC), Accessed: [2022/8/12],  
941 doi:10.5067/MEASURES/GPCP/DATA304, 2022.



- 942 Janowiak, J. E., Gruber, A., Kondragunta, C. R., Livezey, R. E., and Huffman, G. J.: A comparison of the NCEPNCAR  
943 reanalysis precipitation and the GPCP rain gauge satellite combined dataset with observational error considerations, *J. Climate*,  
944 11, 2960–2979, doi:10.1175/1520-0442, 1998.
- 945 Jasechko, S., Sharp, Z. D., Gibson, J. J., Birks, S. J., Yi, Y., and Fawcett, P. J.: Terrestrial water fluxes dominated by  
946 transpiration, *Nature*, 496, 347–350, 2013.
- 947 Jung, M., Koirala, S., Weber, U., Ichii, K., Gans, F., Camps-Valls, G., Papale, D., Schwalm, C., Tramontana, G., and Reichstein,  
948 M.: The FLUXCOM ensemble of global land-atmosphere energy fluxes, *Sci. Data*, 6, 74, doi:10.1038/s41597-019-0076-8,  
949 2019.
- 950 Kanamitsu, M., Ebisuzaki, W., Woollen, J., Yang, S. K., Hnilo, J. J., Fiorino, M., and Potter, G. L.: NCEP-DOE AMIP-II  
951 reanalysis (R-2), *B. Am. Meteorol. Soc.*, 83, 1631–1643, doi:10.1175/BAMS-83-11-1631, 2002.
- 952 Kistler, R., Collins, W., Saha, S., White, G., Woollen, J., Kalnay, E., Chelliah, M., Ebisuzaki, W., Kanamitsu, M., Kousky, V.,  
953 van den Dool, H., Jenne, R., and Fiorino, M.: The NCEP-NCAR 50-year reanalysis: monthly means CD-ROM and  
954 documentation, *B. Am. Meteorol. Soc.*, 82, 247–267, doi:10.1175/1520-0477, 2001.
- 955 Kornfeld, R. P., Arnold, B. W., Gross, M. A., Dahya, N. T., Klipstein, W. M., Gath, P. F., and Bettadpur, S.: GRACE-FO: the  
956 gravity recovery and climate experiment follow-on mission, *J. Spacecraft Rockets*, 56, 931–951, doi:10.2514/1.A34326, 2019.
- 957 Koster, R. D., Dirmeyer, P. A., Guo, Z., Bonan, G., Chan, E., Cox, P., Gordon, C. T., Kanae, S., Kowalczyk, E., Lawrence,  
958 D., Liu, P., Lu, C.-H., Malyshev, S., McAvaney, B., Mitchell, K., Mocko, D., Oki, T., Oleson, K., Pitman, A., Sud, Y. C.,  
959 Taylor, C. M., Verseghy, D., Vasic, R., Xue, Y., and Yamada, T.: Regions of strong coupling between soil moisture and  
960 precipitation, *Science*, 305, 1138–1140, <https://doi.org/10.1126/science.1100217>, 2004.
- 961 Lehmann, F., Vishwakarma, B. D., and Bamber, J.: How well are we able to close the water budget at the global scale? *Hydrol.*  
962 *Earth Syst. Sci.*, 26, 35–54, doi:10.5194/hess-26-35-2022, 2022.
- 963 Li, X., Long, D., Han, Z., Scanlon, B. R., Sun, Z., Han, P., and Hou, A.: Evapotranspiration estimation for Tibetan Plateau  
964 headwaters using conjoint terrestrial and atmospheric water balances and multisource remote sensing, *Water Resour. Res.*, 55,  
965 doi:10.1029/2019WR025196, 2019.
- 966 Li, X. P., Wang, L., Chen, D. L., Yang, K., and Wang, A. H.: Seasonal evapotranspiration changes (1983–2006) of four large  
967 basins on the Tibetan Plateau, *J. Geophys. Res.*, 119, 13079–13095, 2014.
- 968 Liu, W., Wang, L., Zhou, J., Li, Y., Sun, F., Fu, G., Li, X., and Sang, Y.-F.: A worldwide evaluation of basin-scale  
969 evapotranspiration estimates against the water balance method, *J. Hydrol.*, 538, 82–95, doi:10.1016/j.jhydrol.2016.04.006,  
970 2016.
- 971 Long, D., Longuevergne, L., and Scanlon, B. R.: Uncertainty in evapotranspiration from land surface modeling, remote sensing,  
972 and GRACE satellites, *Water Resour. Res.*, 50, 1131–1151, doi:10.1002/2013WR014581, 2014.
- 973 Long, D., Longuevergne, L., and Scanlon, B. R.: Global analysis of approaches for deriving total water storage changes from  
974 GRACE satellites, *Water Resour. Res.*, 51, 2574–2594, doi:10.1002/2014WR016853, 2015.



- 975 Loomis, B. D., Rachlin, K. E. and Luthcke, S. B.: Improved earth oblateness rate reveals increased ice sheet losses and mass-  
976 driven sea level rise, *Geophys. Res. Lett.*, 46, 6910–6917, 2019.
- 977 Muñoz-Sabater, J., Dutra, E., Agustí-Panareda, A., Albergel, C., Arduini, G., Balsamo, G., Boussetta, S., Choulga, M.,  
978 Harrigan, S., Hersbach, H., Martens, B., Miralles, D. G., Piles, M., Rodríguez-Fernández, N. J., Zsoter, E., Buontempo, C.,  
979 and Thépaut, J.-N.: ERA5-Land: a state-of-the-art global reanalysis dataset for land applications, *Earth Syst. Sci. Data*, 13,  
980 4349–4383, doi:10.5194/essd-13-4349-2021, 2021.
- 981 Kobayashi, S., Ota, Y., Harada, Y., Ebata, A., Moriya, M., Onoda, H., Onogi, K., Kamahori, H., Kobayashi, C., and Endo, H.:  
982 The JRA-55 reanalysis: General specifications and basic characteristics, *J. Meteorol. Soc. Jpn.-Ser. II*, 93, 5–48,  
983 doi:10.2151/jmsj.2015-001, 2015.
- 984 Martens, B., Miralles, D. G., Lievens, H., van der Schalie, R., de Jeu, R. A. M., Fernández-Prieto, D., Beck, H. E., Dorigo, W.  
985 A., and Verhoest, N. E. C.: GLEAM v3: satellite-based land evaporation and root-zone soil moisture, *Geosci. Model Dev.*, 10,  
986 1903–1925, doi:10.5194/gmd-10-1903-2017, 2017.
- 987 Miralles, D. G., Brutsaert, W., Dolman, A., and Gash, J. H.: On the use of the term “evapotranspiration”, *Water Resour. Res.*,  
988 56, e2020WR028055, <https://doi.org/10.1029/2020WR028055>, 2020.
- 989 Miralles, D. G., Jiménez, C., Jung, M., Michel, D., Ershadi, A., McCabe, M. F., Hirschi, M., Martens, B., Dolman, A. J.,  
990 Fisher, J. B., Mu, Q., Seneviratne, S. I., Wood, E. F., and Fernández-Prieto, D.: The WACMOS-ET project – Part 2: Evaluation  
991 of global terrestrial evaporation data sets, *Hydrol. Earth Syst. Sci.*, 20, 823–842, <https://doi.org/10.5194/hess-20-823-2016>,  
992 2016.
- 993 Mu, Q., Zhao, M., and Running, S. W.: Improvements to a MODIS global terrestrial evapotranspiration algorithm, *Remote  
994 Sens. Environ.*, 115, 1781–1800, doi:10.1016/j.rse.2011.02.019, 2011.
- 995 Müller Schmied, H., Cáceres, D., Eisner, S., Flörke, M., Herbert, C., Niemann, C., Peiris, T. A., Popat, E., Portmann, F. T.,  
996 Reinecke, R., Schumacher, M., Shadkam, S., Telteu, C.-E., Trautmann, T., and Döll, P.: The global water resources and use  
997 model WaterGAP v2.2d: model description and evaluation, *Geosci. Model Dev.*, 14, 1037–1079, doi:10.5194/gmd-14-1037-  
998 2021, 2021.
- 999 Okamoto, K., Ushio, T., Iguchi, T., Takahashi, N., and Iwanami, K.: The global satellite mapping of precipitation (GSMaP)  
1000 project, in: *Proceedings, 2005 IEEE International Geoscience and Remote Sensing Symposium, IGARSS'05*, vol. 5, 3414–  
1001 3416, IEEE, 29–29 July 2005, Seoul, 2005.
- 1002 Oki, T., and Kanae, S.: Global hydrological cycles and world water resources, *Science*, 313, 1068–1072, 2006.
- 1003 Pan, Y., Zhang, C., Gong, H., Yeh, P. J. F., Shen, Y., Guo, Y., Huang, Z., and Li, X.: Detection of human-induced  
1004 evapotranspiration using GRACE satellite observations in the Haihe River basin of China, *Geophys. Res. Lett.*, 44, 190–199,  
1005 doi:10.1002/2016gl071287, 2017.
- 1006 Pascolini-Campbell, M. A., Reager, J. T., and Fisher, J. B.: GRACE-based mass conservation as a validation target for basin-  
1007 scale evapotranspiration in the contiguous United States, *Water Resour. Res.*, 56, e2019WR026594,  
1008 doi:10.1029/2019WR026594, 2020.



- 1009 Qi, W., Liu, J. G., and Chen, D. L.: Evaluations and improvements of GLDAS2.0 and GLDAS2.1 forcing data's applicability  
1010 for basin scale hydrological simulations in the Tibetan Plateau, *J. Geophys. Res.-Atmos.*, 123, 13128–13148,  
1011 doi:10.1029/2018jd029116, 2018.
- 1012 Qi, W., Liu, J., Yang, H., Zhu, X., Tian, Y., Jiang, X., Huang, X., and Feng, L.: Large uncertainties in runoff estimations of  
1013 GLDAS versions 2.0 and 2.1 in China, *Earth Space Sci.*, 7, e2019EA000829, doi:10.1029/2019EA000829, 2020.
- 1014 Reichle, R. H., Liu, Q., Koster, R. D., Draper, C. S., Mahanama, S. P. P., and Partyka, G. S.: Land surface precipitation in  
1015 MERRA-2, *J. Climate*, 30, 1643–1664, doi:10.1175/JCLI-D-16-0570.1, 2017.
- 1016 Rodell, M., Famiglietti, J.S., Chen, J., Seneviratne, S.I., Viterbo, P., Holl, S., and Wilson, C.R.: Basin scale estimates of  
1017 evapotranspiration using GRACE and other Observations, *Geophys. Res. Lett.*, 31, L20504, doi:10.1029/2004GL020873,  
1018 2004.
- 1019 Rodell, M., Velicogna, I., and Famiglietti, J. S.: Satellite-based estimates of groundwater depletion in India, *Nature*, 460, pp.  
1020 999–1002, 2009.
- 1021 Rodell, M., McWilliams, E. B., Famiglietti, J. S., Beaudoing, H. K., and Nigro, J.: Estimating evapotranspiration using an  
1022 observation based terrestrial water budget, *Hydrol. Process.*, 25, 4082–4092, doi:10.1002/hyp.8369, 2011.
- 1023 Rodell, M., Beaudoing, H. K., L'Ecuyer, T. S., Olson, W. S., Famiglietti, J. S., Houser, P. R., Adler, R., Bosilovich, M. G.,  
1024 Clayson, C. A., Chambers, D., Clark, E., Fetzer, E. J., Gao, X., Gu, G., Hilburn, K., Huffman, G. J., Lettenmaier, D. P., Liu,  
1025 W. T., Robertson, F. R., Schlosser, C. A., Sheffield, J., and Wood, E. F.: The observed state of the water cycle in the early  
1026 twenty-first century, *J. Climate*, 28, 8289–8318, doi:10.1175/JCLI-D-14-00555.1, 2015.
- 1027 Rodell, M., Famiglietti, J. S., Wiese, D. N., Reager, J. T., Beaudoing, H. K., Landerer, F. W., and Lo, M.-H.: Emerging trends  
1028 in global freshwater availability, *Nature*, 557, 651–659, <https://doi.org/10.1038/s41586-018-0123-1>, 2018.
- 1029 Ramillien, G., Frappart, F., Güntner, A., Ngo-Duc, T., Cazenave, A., and Laval, K.: Time variations of the regional  
1030 evapotranspiration rate from Gravity Recovery and Climate Experiment (GRACE) satellite gravimetry, *Water Resour. Res.*,  
1031 42, W10403, doi:10.1029/2005WR004331, 2006.
- 1032 Saha, S., Moorthi, S., Pan, H.-L., Wu, X., Wang, J., Nadiga, S., Tripp, P., Kistler, R., Woollen, J., Behringer, D., Liu, H.,  
1033 Stokes, D., Grumbine, R., Gayno, G., Wang, J., Hou, Y.-T., Chuang, H.-y., Juang, H.-M. H., Sela, J., Iredell, M., Treadon, R.,  
1034 Kleist, D., Delst, P. V., Keyser, D., Derber, J., Ek, M., Meng, J., Wei, H., Yang, R., Lord, S., Dool, H. v. d., Kumar, A., Wang,  
1035 W., Long, C., Chelliah, M., Xue, Y., Huang, B., Schemm, J.-K., Ebisuzaki, W., Lin, R., Xie, P., Chen, M., Zhou, S., Higgins,  
1036 W., Zou, C.-Z., Liu, Q., Chen, Y., Han, Y., Cucurull, L., Reynolds, R. W., Rutledge, G., and Goldberg, M.: The NCEP climate  
1037 forecast system reanalysis, *B. Am. Meteorol. Soc.*, 91, 1015–1058, doi:10.1175/2010bams3001.1, 2010.
- 1038 Save, H., Bettadpur, S., and Tapley, B. D.: High-resolution CSR GRACE RL05 mascons, *J. Geophys. Res.-Solid Earth*, 121,  
1039 7547–7569, doi:10.1002/2016JB013007, 2016.
- 1040 Scanlon, B. R., Zhang, Z., Save, H., Sun, A. Y., Müller Schmied, H., van Beek, L. P. H., Wiese, D. N., Wada, Y., Long, D.,  
1041 Reedy, R. C., Longuevergne, L., Döll, P., and Bierkens, M. F. P.: Global models underestimate large decadal declining and



- 1042 rising water storage trends relative to GRACE satellite data, *Proc. Natl. Acad. Sci. USA*, 115, E1080–E1089,  
1043 doi:10.1073/pnas.1704665115, 2018.
- 1044 Slivinski, L. C., Compo, G. P., Whitaker, J. S., Sardeshmukh, P. D., Giese, B. S., McColl, C., Allan, R., Yin, X., Vose, R.,  
1045 Titchner, H., Kennedy, J., Spencer, L. J., Ashcroft, L., Brönnimann, S., Brunet, M., Camuffo, D., Cornes, R., Cram, T. A.,  
1046 Crouthamel, R., Domínguez-Castro, F., Freeman, J. E., Gergis, J., Hawkins, E., Jones, P. D., Jourdain, S., Kaplan, A., Kubota,  
1047 H., Le Blancq, F., Lee, T., Lorrey, A., Luterbacher, J., Maugeri, M., Mock, C. J., Moore, G. K., Przybylak, R., Pudmenzky,  
1048 C., Reason, C., Slonosky, V. C., Smith, C., Tinz, B., Trewin, B., Valente, M. A., Wang, X. L., Wilkinson, C., Wood, K., and  
1049 Wyszynski, P.: Towards a more reliable historical reanalysis: Improvements for version 3 of the twentieth century reanalysis  
1050 system, *Q. J. Roy. Meteor. Soc.*, 145, 2876–2908, doi:10.1002/qj.3598, 2019.
- 1051 Schneider, U., Becker, A., Finger, P., Rustemeier, E. and Ziese, M.: GPCP full data monthly product Version 2020 at 0.25°:  
1052 monthly land-surface precipitation from rain-gauges built on GTS-based and Historical Data, 2020.
- 1053 Sen, P. K.: Estimates of the Regression Coefficient Based on Kendall's Tau, *J. Am. Stat. Assoc.*, 63, 1379–1389, 1968.
- 1054 Shumilova, O., Tockner, K., Thieme, M., Koska, A. and Zarfl, C.: Global water transfer megaprojects: A potential solution  
1055 for the water-food-energy nexus? *Front. Environ. Sci.*, 6, 2018.
- 1056 Sneeuw, N., Lorenz, C., Devaraju, B., Tourian, M. J., Riegger, J., Kunstmann, H., and Bárdossy, A.: Estimating Runoff Using  
1057 Hydro-Geodetic Approaches, *Surv. Geophys.*, 35, 1333–1359, <https://doi.org/10.1007/s10712-014-9300-4>, 2014.
- 1058 Swann, A. L. S. and Koven, C. D.: A direct estimate of the seasonal cycle of evapotranspiration over the Amazon Basin, *J.*  
1059 *Hydrometeorol.*, 18, 2173–2185, <https://doi.org/10.1175/JHM-D-17-0004.1>, 2017.
- 1060 Syed, T. H., Famiglietti, J. S., Chambers, D. P., Willis, J. K., and Hilburn, K.: Satellite-based global-ocean mass balance  
1061 estimates of interannual variability and emerging trends in continental freshwater discharge, *P. Natl. Acad. Sci. USA*, 107,  
1062 17916–17921, 2010.
- 1063 Syed, T. H., Webster, P. J. M and Famiglietti, J. S.: Assessing variability of evapotranspiration over the Ganga River basin  
1064 using water balance computations, *Water Resour. Res.*, 50, 2551–2565, doi:10.1002/2013WR013518, 2014.
- 1065 Swenson, S. and Wahr, J.: Post-processing removal of correlated errors in GRACE data, *Geophys. Res. Lett.*, 33, L08402,  
1066 doi:10.1029/2005GL025285, 2006.
- 1067 Tapley, B. D., Bettadpur, S., Watkins, M., and Reigber, C.: The gravity recovery and climate experiment: mission overview  
1068 and early results, *Geophys. Res. Lett.*, 31, L09607, doi: 10.1029/2004GL019920, 2004
- 1069 Tapley, B. D., Bettadpur, S., Ries, J. C., Thompson, P. F., and Watkins, M. M.: GRACE measurements of mass variability in  
1070 the earth system, *Science*, 305, 503–505, <https://doi.org/10.1126/science.1099192>, 2004.
- 1071 Vishwakarma, B. D., Devaraju, B., and Sneeuw, N.: What Is the Spatial Resolution of grace Satellite Products for Hydrology?  
1072 *Remote Sens.*, 10, 852. doi:10.3390/rs10060852, 2018.
- 1073 Vishwakarma, B. D., Horwath, M., Devaraju, B., Groh, A., and Sneeuw, N.: A data-driven approach for repairing the  
1074 hydrological catchment signal damage due to filtering of GRACE products: repairing signal damage due to filtering, *Water*  
1075 *Resour. Res.*, 53, 9824–9844, doi:10.1002/2017WR021150, 2017.



- 1076 Vishwakarma B. D., Bates P., Sneeuw N., Westaway R. M., and Bamber J. L.: Re-assessing global water storage trends from  
1077 GRACE time series, *Environ. Res. Lett.*, 16(3): 034005, doi:10.1088/1748-9326/abd4a9, 2021.
- 1078 Vishwakarma B. D.: Monitoring Droughts From GRACE, *Front. Environ. Sci.*, 8: 584690, 2020.
- 1079 Wahr, J., Molenaar, M., and Bryan, F.: Time variability of the earth's gravity field: hydrological and oceanic effects and their  
1080 possible detection using GRACE, *J. Geophys. Res.*, 103, 30205–30229, doi:10.1029/98JB02844, 1998.
- 1081 Wan, Z., Zhang, K., Xue, X., Hong, Z., Hong, Y., and Gourley, J. J.: Water balance-based actual evapotranspiration  
1082 reconstruction from ground and satellite observations over the conterminous United States, *Water Resour. Res.*, 51, 6485–  
1083 6499, <https://doi.org/10.1002/2015WR017311>, 2015.
- 1084 Wang, K. C. and Dickinson, R. E.: A review of global terrestrial evapotranspiration: observation, modeling, climatology, and  
1085 climatic variability, *Rev. Geophys.*, 50, RG2005, <https://doi.org/10.1029/2011RG000373>, 2012.
- 1086 Wang, W., Xing, W., and Shao, Q.: How large are uncertainties in future projection of reference evapotranspiration through  
1087 different approaches? *J. Hydrol.*, 524, 696–700, <https://doi.org/10.1016/j.jhydrol.2015.03.033>, 2015.
- 1088 Wang, W., Cui, W., Wang, X. J., and Chen, X.: Evaluation of GLDAS-1 and GLDAS-2 forcing data and Noah model  
1089 simulations over China at the monthly scale, *J. hydrometeor.*, 17, 2815–2833, 2016.
- 1090 Watkins, M. M., Wiese, D. N., Yuan, D.-N., Boening, C., and Landerer, F. W.: Improved methods for observing earth's time  
1091 variable mass distribution with GRACE using spherical cap mascons, *J. Geophys. Res.-Solid Earth*, 120, 2648–2671, 2015.
- 1092 Weedon, G. P., Balsamo, G., Bellouin, N., Gomes, S., Best, M. J., and Viterbo, P.: The WFDEI meteorological forcing data  
1093 set: WATCH Forcing Data methodology applied to ERA-Interim reanalysis data, *Water Resour. Res.*, 50, 7505–7514, 2014.
- 1094 Wiese, D. N., Landerer, F. W. and Watkins, M. M.: Quantifying and reducing leakage errors in the JPL RL05M GRACE  
1095 mascon solution, *Water Resour. Res.*, 52, 7490–7502, 2016.
- 1096 Xie, P. and Arkin, P. A.: Global precipitation: A 17-year monthly analysis based on gauge observations, satellite estimates and  
1097 numerical model outputs, *B. Am. Meteorol. Soc.*, 78, 2539–2558, 1997.
- 1098 Xiong, J., Abhishek, Pan Y., Gionata, G., and Guo, S.: ET-WB: the water balance estimations of terrestrial evaporation over  
1099 global basins [dataset], [doi:10.5281/zenodo.7314920](https://doi.org/10.5281/zenodo.7314920), 2023.
- 1100 Xiong, J., Abhishek, Guo, S., and Kinouchi, T.: Leveraging machine learning methods to quantify 50 years of dwindling  
1101 groundwater in India, *Sci. Total Environ.*, 835, 155474, 2022a.
- 1102 Xiong, J., Guo, S., Abhishek, Chen, J., and Yin, J.: Global evaluation of the “dry gets drier, and wet gets wetter” paradigm  
1103 from a terrestrial water storage change perspective, *Hydrol. Earth Syst. Sci.*, 26, 6457–6476, doi:10.5194/hess-26-6457-2022,  
1104 2022b.
- 1105 Xue, B. L., Wang, L., Li, X., Yang, K., Chen, D., and Sun, L.: Evaluation of evapotranspiration estimates for two river basins  
1106 on the Tibetan Plateau by a water balance method, *J. Hydrol.*, 492, 290–297, 2013.
- 1107 Yang, Y. T., Long, D., and Shang, S. H.: Remote estimation of terrestrial evapotranspiration without using meteorological  
1108 data, *Geophys. Res. Lett.*, 40, 3026–3030, doi:10.1002/grl.50450, 2013.



- 1109 Yang, Y. T. and Shang, S. H.: A hybrid dual-source scheme and trapezoid framework-based evapotranspiration model (HTEM)  
1110 using satellite images: Algorithm and model test, *J. Geophys. Res.-Atmos.*, 118, 2284–2300, doi:10.1002/jgrd.50259, 2013.
- 1111 Yang, T., Ding, J., Liu, D., Wang, X., and Wang, T.: Combined use of multiple drought indices for global assessment of dry  
1112 gets drier and wet gets wetter paradigm, *J. Clim.*, 32, 737–748, doi:10.1175/JCLI-D-18-0261.1, 2019.
- 1113 Yi, S. and Sneeuw, N.: Filling the data gaps within GRACE missions using singular spectrum analysis, *J. Geophys. Res. Solid  
1114 Earth*, 126, e2020JB021227, 2021.
- 1115 Yu, L., Qiu, G. Y., Yan, C., Zhao, W., Zou, Z., Ding, J., Qin, L., and Xiong, Y.: A global terrestrial evapotranspiration product  
1116 based on the three-temperature model with fewer input parameters and no calibration requirement, *Earth Syst. Sci. Data*, 14,  
1117 3673–3693, doi:10.5194/essd-14-3673-2022, 2022.
- 1118 Zeng, Z., Piao, S., Lin, X., Yin, G., Peng, S., Ciais, P., and Myneni, R. B.: Global evapotranspiration over the past three  
1119 decades: estimation based on the water balance equation combined with empirical models, *Environ. Res. Lett.*, 7, 014026,  
1120 doi:10.1088/1748-9326/7/1/014026, 2012.
- 1121 Zhang, K., Kimball, J. S., Nemani, R. R., and Running, S. W.: A continuous satellite-derived global record of land surface  
1122 evapotranspiration from 1983 to 2006, *Water Resour. Res.*, 46, W09522, doi:10.1029/2009WR008800, 2010.
- 1123 Zhong, Y., Zhong, M., Mao, Y., and Ji, B.: Evaluation of evapotranspiration for exoreic catchments of China during the  
1124 GRACE Era: from a water balance perspective, *Remote Sens.*, 12, 511, doi:10.3390/rs12030511, 2020.
- 1125